



The California Legacy Survey. V. Chromospheric Activity Cycles in Main-sequence Stars

Howard Isaacson^{1,2}, Andrew W. Howard³, Benjamin Fulton⁴, Erik A. Petigura⁵, Lauren M. Weiss⁶,
 Stephen R. Kane^{2,7}, Brad Carter², Corey Beard^{8,20}, Steven Giacalone^{3,19}, Judah Van Zandt⁵,
 Joseph M. Akana Murphy^{9,20}, Fei Dai^{3,10,19}, Ashley Chontos^{11,12,18}, Alex S. Polanski¹³, Malena Rice¹⁴,
 Jack Lubin^{5,8}, Casey Brinkman¹¹, Ryan A. Rubenzahl^{3,19,21}, Sarah Blunt¹⁵, Samuel W. Yee^{12,18},
 Mason G. MacDougall⁵, Paul A. Dalba^{9,20}, Dakotah Tyler⁵, Aida Behmar¹⁶, Isabel Angelo⁵, Daria Pidhorodetska^{7,20},
 Andrew W. Mayo^{1,17}, Rae Holcomb⁸, Emma V. Turtelboom¹, Michelle L. Hill⁷, Luke G. Bouma³,
 Jingwen Zhang^{11,20}, Ian J. M. Crossfield¹³, and Nicholas Saunders¹¹

¹ 501 Campbell Hall, University of California at Berkeley, Berkeley, CA 94720, USA; hisaacson@berkeley.edu

² Centre for Astrophysics, University of Southern Queensland, Toowoomba, QLD, Australia

³ Department of Astronomy, California Institute of Technology, Pasadena, CA 91125, USA

⁴ NASA Exoplanet Science Institute/IPAC, California Institute of Technology, MC 314-6, 1200 E. California Blvd., Pasadena, CA 91125, USA

⁵ Department of Physics & Astronomy, University of California Los Angeles, Los Angeles, CA 90095, USA

⁶ Department of Physics and Astronomy, University of Notre Dame, Notre Dame, IN 46556, USA

⁷ Department of Earth and Planetary Sciences, University of California, Riverside, CA 92521, USA

⁸ Department of Physics & Astronomy, University of California Irvine, Irvine, CA 92697, USA

⁹ Department of Astronomy and Astrophysics, University of California, Santa Cruz, CA 95064, USA

¹⁰ Division of Geological and Planetary Sciences, California Institute of Technology, 1200 E. California Blvd., Pasadena, CA 91125, USA

¹¹ Institute for Astronomy, University of Hawai'i, 2680 Woodlawn Dr., Honolulu, HI 96822, USA

¹² Department of Astrophysical Sciences, Princeton University, 4 Ivy Ln., Princeton, NJ 08544, USA

¹³ Department of Physics & Astronomy, University of Kansas, 1082 Malott, 1251 Wescoe Hall Dr., Lawrence, KS 66045, USA

¹⁴ Department of Astronomy, Yale University, New Haven, CT 06511, USA

¹⁵ Center for Interdisciplinary Exploration and Research in Astrophysics (CIERA) and Department of Physics and Astronomy, Northwestern University, Evanston, IL 60208, USA

¹⁶ Department of Astrophysics, American Museum of Natural History, 200 Central Park W., Manhattan, NY 10024, USA

¹⁷ Centre for Star and Planet Formation, Natural History Museum of Denmark & Niels Bohr Institute, University of Copenhagen, Øster Voldgade 5-7, DK-1350 Copenhagen K., Denmark

Received 2024 May 12; revised 2024 June 25; accepted 2024 July 8; published 2024 September 30

Abstract

We present optical spectroscopy of 710 solar neighborhood stars collected over 20 years to catalog chromospheric activity and search for stellar activity cycles. The California Legacy Survey stars are amenable to exoplanet detection using precise radial velocities, and we present their Ca II H and K time series as a proxy for stellar and chromospheric activity. Using the High Resolution Echelle Spectrometer at Keck Observatory, we measured stellar flux in the cores of the Ca II H and K lines to determine S -values on the Mount Wilson scale and the $\log(R'_{\text{HK}})$ metric, which is comparable across a wide range of spectral types. From the 710 stars, with 52,372 observations, 285 stars were sufficiently sampled to search for stellar activity cycles with periods of 2–25 yr, and 138 stars showed stellar cycles of varying length and amplitude. S -values can be used to mitigate stellar activity in the detection and characterization of exoplanets. We used them to probe stellar dynamos and to place the Sun's magnetic activity into context among solar neighborhood stars. Using precise stellar parameters and time-averaged activity measurements, we found tightly constrained cycle periods as a function of stellar temperature between $\log(R'_{\text{HK}})$ of -4.7 and -4.9 , a range of activity in which nearly every star has a periodic cycle. These observations present the largest sample of spectroscopically determined stellar activity cycles to date.

Unified Astronomy Thesaurus concepts: [Stellar astronomy \(1583\)](#); [Main sequence stars \(1000\)](#); [Time series analysis \(1916\)](#); [Stellar chromospheres \(230\)](#); [Stellar activity \(1580\)](#); [Stellar evolution \(1599\)](#); [High resolution spectroscopy \(2096\)](#); [Optical telescopes \(1174\)](#)

Materials only available in the online version of record: figure set, machine-readable tables

1. Introduction

Long-term, ground-based spectroscopic surveys are a pathway to understanding the Sun and its planets in the

context of the solar neighborhood and to finding Earth-analog exoplanet systems. Such surveys can probe the depth of the convective zone, detect differential rotation, and track Sunlike stellar activity cycles. Chromospheric activity studies provide fascinating insights into the subsurface layers of stars that are not directly observable. Over the last two decades, these studies have been buoyed by radial velocity (RV) searches for exoplanets due to the collection of time cadence observations that include spectral information that can be used for both measuring precise RVs of stars and monitoring stellar chromospheric activity (Gomes da Silva et al. 2021; Rosenthal et al. 2021, hereafter CLS1).

¹⁸ Henry Norris Russell Fellow.

¹⁹ NSF Astronomy and Astrophysics Postdoctoral Fellow.

²⁰ NASA FINESST Fellow.

²¹ NSF Graduate Research Fellow.



Nightly surveying of the chromospheric activity of nearby stars in the Mount Wilson Observatory HK Project began in 1966 (Wilson 1968) and continued for several decades (Vaughan et al. 1978). This survey detected variable stellar lines and identified the link between the Ca II H and K lines and the solar chromosphere (Eberhard & Schwarzschild 1913). After decades of data collection on F2–M2-type stars—an effort necessary to identify stellar activity cycles in some G0–K5 stars with activity periods similar to the Sun’s 11 yr solar cycle—the results were summarized (Duncan et al. 1991) and the first catalog of stellar activity cycles was published (Baliunas et al. 1995). Out of 111 solar-type stars searched, 52 showed cycles, and 31 were flat or had linear trends. Another 29 stars had nonperiodic, variable activity. The conclusions put the Sun’s activity cycle into the broader perspective of Sunlike stars in the solar neighborhood, showing that stellar activity cycles are common.

Several long-term ground-based surveys have contributed to our understanding of stellar magnetic activity. Identification of stellar activity cycles using Mount Wilson data combined with California Planet Search (CPS) data from the High Resolution Echelle Spectrometer (HIRES) at the W. M. Keck Observatory yielded baselines of 50 yr for 59 stars (Baum et al. 2022). Time-series spectroscopic observations of Sunlike stars include a survey of 800 Southern solar-type stars within 50 pc (Henry et al. 1996) and 143 Sunlike stars from 1996–2007 (Hall et al. 2007). These studies focused on measuring the average stellar variability, not stellar cycles. Fifty-three previously identified activity cycles were analyzed using S -values from the Mount Wilson Observatory HK Project and the High Accuracy Radial Velocity Planet Searcher (HARPS) telescope (Boro Saikia et al. 2018), but even the extended HARPS baseline was insufficient for identifying new stellar activity cycles that span years to decades. See Jeffers et al. (2023) for a comprehensive review of stellar activity cycles.

Stellar activity and planet searches that use the RV technique have contributed to our knowledge of Jupiter-mass planets with orbital periods of more than 10 yr and to the identification of solar-like stellar cycles (Wright et al. 2008; Fulton et al. 2021). Wright et al. (2004) and Isaacson & Fischer (2010) presented activity catalogs from Keck/HIRES and began to quantify the relationship between RV jitter and chromospheric activity. Luhn et al. (2020) examined 600 CPS stars to make RV jitter assessments that included dependence on stellar surface gravity. A summary of the ground-based spectroscopic survey of the AMBRE-HARPS sample (Gomes da Silva et al. 2021) resulted in an activity catalog of planet search stars in the Southern Hemisphere, with stellar activity time-series analysis forthcoming. Detecting Jupiter analogs requires forward-thinking surveys and understanding their dynamical impact in multiplanet systems will inform the study of solar-like planetary systems (Kane 2023).

In an analysis of Southern Hemisphere planet search stars similar to the Northern Hemisphere sample presented here, Lovis et al. (2011) analyzed seven years of HARPS S -values for 304 FGK-type stars and presented a catalog of 99 magnetic cycles and an analysis of the stellar activity impact on precise RVs. Using the H α line as an activity metric Robertson et al. (2013) searched 93 K- and M-type stars using the High Resolution Spectrograph on the Hobby–Eberly Telescope at McDonald Observatory and identified examples of how activity cycles can mimic those of giant planets. These two catalogs

provide examples of how planet search data has been used to study magnetic activity.

Only with long-term baselines of activity and RVs are the periodic signals of planets distinguished from quasiperiodic activity signals. In some cases, a stellar activity cycle is correlated with the RVs, making the planet interpretation ambiguous (Rosenthal et al. 2021). Kane et al. (2016) identified a stellar activity cycle in HD 99492, a planet-hosting system, while Dragomir et al. (2012) found a photometric activity cycle. Correlations between RVs and S -values over a single period of the planet’s orbit or the stellar activity cycle are difficult to disentangle (Wright et al. 2008; Fulton et al. 2015). But if the baseline is extended sufficiently, the activity cycle may go out of phase, while a planet will maintain strict periodicity (Wright 2016). Stellar activity cycles have been probed by other spectral features that are sensitive to activity. The M dwarf GJ 328 has a confirmed planet along with a stellar activity cycle that was identified with H α line measurements. The CARMENES planet search, which focuses on M dwarfs, has produced a catalog of $\log(R'_{\text{HK}})$ measurements to assist in the interpretation of planet candidates (Perdelwitz et al. 2021).

Wide-field, space-based photometry is now available to search for transiting planets, measure stellar rotation periods, and monitor stellar activity. Such photometry is particularly useful for the determination of stellar rotation periods (McQuillan et al. 2014; Angus et al. 2018), and it has revolutionized rotation studies. Kepler data can be searched for stellar activity cycles, with thousands of cycle candidates (Shen et al. 2022), but the four-year duration of the Kepler mission makes it difficult for us to find solar-like cycles.

Long-term ground-based photometry can be used to find stellar activity cycles, but it is only sensitive to cycles for stars with large spot coverage such as M dwarfs. Irving et al. (2023) examined activity cycles for a collection of M dwarf stars. The coolest M dwarfs, M4 and later, require a different mechanism for magnetic field generation than solar-type stars since they lack a radiative–convective boundary. Spectral analyses of the Ca II H and K lines probe the chromosphere and the magnetic activity below the observable stellar surface, which are complementary to the results of photometric surveys. Photometric studies of activity cycles in M dwarfs have identified cycles in fully convective M dwarfs with masses as low as $0.12 M_{\odot}$ (Savanov 2012; Suárez Mascareño et al. 2016, 2018; Wargelin et al. 2017).

Ground-based photometric surveys have been used to calibrate the age–activity–rotation relationship (Barnes 2007; Mamajek & Hillenbrand 2008) by correlating the stellar rotation periods of open clusters with well-determined ages. Time-averaged chromospheric flux measurements have been used to parameterize the physical mechanisms at work below the observable stellar photosphere. The Rossby number, the ratio of the rotation period to the convective turnover time (Noyes et al. 1984), is the standard metric for quantifying magnetic activity and its relationship to stellar rotation.

Observations of stellar rotation periods, combined with stellar activity cycles, are fleshing out the magnetic activity evolution of stars as their rotation periods decline over time through weakened magnetic braking (van Saders et al. 2016; David et al. 2022; Metcalfe et al. 2022). By combining Ca II H and K measurements with rotation periods, and direct measurements of the magnetic field through spectropolarimetry (Marsden et al. 2014; Metcalfe et al. 2024), more complete

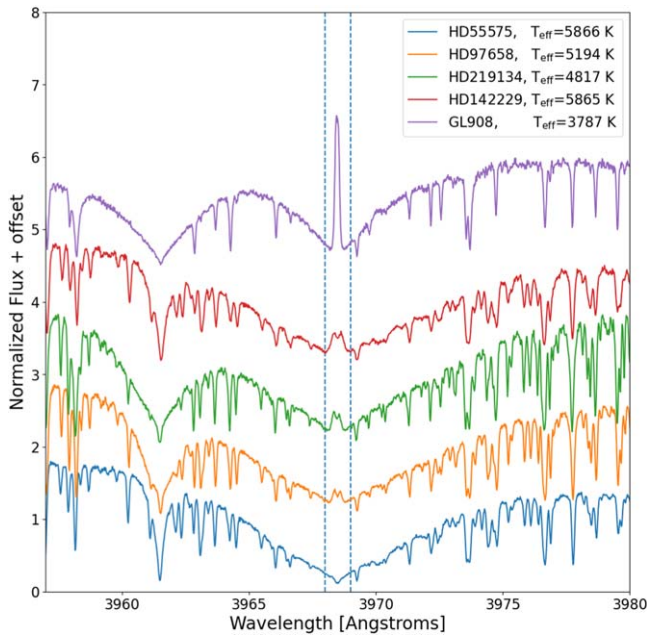


Figure 1. Ca H lines for a variety of effective temperatures from our survey, offset vertically for clarity. The dashed lines mark the center of the extracted flux region for the H line. From bottom to top: HD 55575 ($T_{\text{eff}} = 5866$ K, S -value = 0.156), HD 97658 ($T_{\text{eff}} = 5194$ K, S -value = 0.186), HD 219134 ($T_{\text{eff}} = 4817$ K, S -value = 0.246), HD 142229 ($T_{\text{eff}} = 5865$ K, S -value = 0.364), and GL 908 ($T_{\text{eff}} = 3787$ K, S -value = 0.54).

explanations of the stellar dynamo are now coming into focus. We add to the observational evidence that can be used to understand main-sequence magnetic changes and potentially to explain weakened magnetic braking.

We present 20 years of stellar chromospheric activity time series for 710 nearby (median distance of 30 pc) main-sequence FGKM stars, analyze average activity in terms of fundamental stellar properties, and search for activity cycles like the Sun’s 11 yr cycle. Section 2 discusses the observations and data quality. Section 3 discusses the CLS1 stellar sample and compares it to those of previously published works. Section 4 discusses our 285-star sample that is searched for cycles. Section 5 explores the activity cycles in terms of the stellar properties for 138 stars with detected cycles and Section 6 reveals the relationship between cycle period and T_{eff} .

2. Observations

2.1. Data Source and Quality

The CLS1 paper provided RVs measured from data collected from the middle of three detectors (4976–6421 Å), and the S -values were simultaneously measured using data from the blue detector (3642–4797 Å). We used an updated raw reduction that converted 2D spectra to 1D spectra (Howard et al. 2010). This work improves the quality of the S -values as compared to CLS1 by using a restricted extraction width of eight pixels to reduce sky emission and scattered light contamination and by making additional quality controls. A sample of Ca H line profiles for properly reduced spectra in good seeing are shown in Figure 1.

HIRES spectra were collected with a variety of decker apertures. The primary science deckers for CPS are B5 ($0''.87 \times 5''$) and C2 ($0''.87 \times 14''$), which provide a resolution of 60,000. Two other deckers, B1 ($0''.5 \times 5''$) and B3

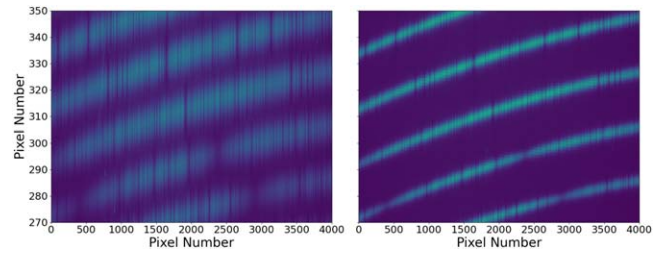


Figure 2. Two raw images of HD 141399 showing the Ca II H and K region. Left: seeing measured to be $2''.5$. Right: seeing measured to be $0''.9$. The extraction width in the cross-dispersion (vertical) direction is limited to eight pixels.

($0''.5 \times 14''$), are used for templates and result in a resolution of 80,000. The C2 decker began operation in 2009 June, when the typical visual magnitude of RV targets changed from $V \sim 8$, for nearby-star surveys, to $V \sim 12$, for follow-up of Kepler planet-host stars. Sky contamination became a limiting factor in RV precision, requiring observations with the C2 decker (Marcy et al. 2014), at the occasional expense of useful S -value measurements. The B5 decker was used for stars brighter than $V \sim 10$, and C2 was used for fainter stars and for observations taken during twilight, when CLS1 stars were often observed.

The height of the C2 and B3 deckers allows for simultaneous observations of sky pixels and causes order overlap on the middle CCD, and increasing overlap blueward. Echelle spectrographs with cross-dispersing gratings have blue orders closer together and red orders with larger separation, and the opposite is true for cross-dispersing prisms. The raw reduction has been tailored to account for this in the middle detector, resulting in equal RV precision for B5 and C2. For S -values, the additional overlap near the Ca II H and K lines is more problematic and causes degraded quality for observations taken in poor seeing conditions. By measuring the stellar profile in the spatial direction, we calculated the average seeing for each observation. Using chromospherically inactive stars, we identified the upper limit of $1''.6$ to be the critical seeing value required to avoid order-to-order contamination when observing with the C2 or B3 decker (Baum et al. 2022). We excluded S -values with seeing measurements beyond this value from our sample, removing 1549 S -values. The B5 and B1 deckers with their shorter height do not have order overlap and do not have this restriction. Figure 2 shows 2D echellegrams for the star HD 141399 taken in seeing conditions of $2''.5$ and $0''.9$, showing the order overlap that occurs during poor seeing conditions. In addition to the quality control described above, we visually examined exceptionally low S -values and excluded 98 observations with poor extractions.

2.2. S -value Error

We previously adopted the S -value error of 0.002, or 1% per individual observation, by assessing the S -value distribution of HD 10700 (τ Cet), a star with a well-established low level of activity (Isaacson & Fischer 2010). Our extended time baseline yields a dispersion of the HD 10700 S -values of 0.82% (0.00139/0.1675). We identified other stars with very low S -value variation, including HD 55575, our least active star that has a dispersion of $0.0007/0.156 = 0.45\%$. We adopted an S -value error of 0.001 for all observations, a value between the dispersions of HD 10700 and HD 55575. The HARPS-AMBRE survey found a dispersion of 0.83% for HD 10700,

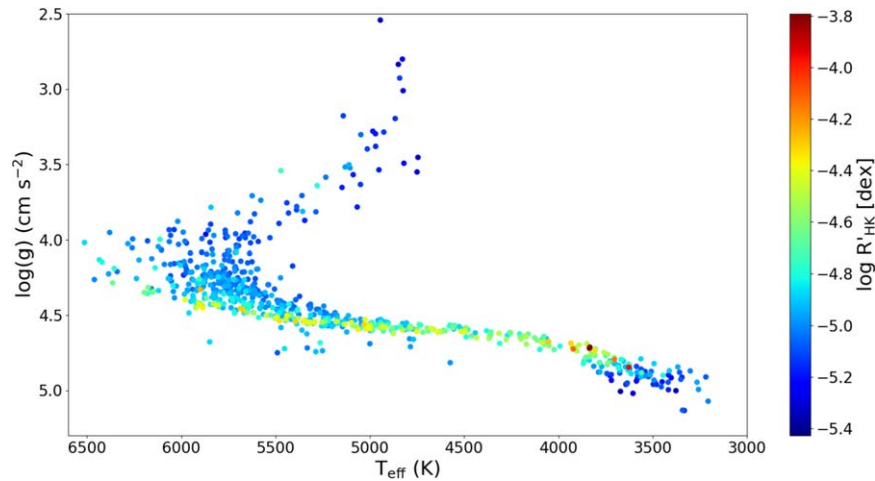


Figure 3. Stellar surface gravity as a function of effective temperature is plotted, with the median $\log(R'_{\text{HK}})$ value for each of the 710 stars in the California Legacy Survey activity sample represented on the color scale. Subgiants are visible at lower $\log(g)$ values, while the few very-low-metallicity subdwarfs in our sample fall below the main sequence. Most stars in our sample are slowly rotating FGKM stars on the main sequence.

showing that this precision level is achievable (Gomes da Silva et al. 2021). We discuss the least active stars in Section 5.6.

2.3. Sampling

The CLS1 survey required 10 RV observations over 8 yr (since 2005) on HIRES (Figure 2 in CLS1) to be included in their analysis. They supplemented their data set with pre-2005 HIRES RVs and Lick Observatory RVs (Fischer et al. 2014). We do not include the Lick Observatory S -values nor the pre-2005 HIRES S -values. We considered adding S -values from the Automated Planet Finder, but there is no additional baseline since the first observations were taken in 2014. Since CLS1 we have collected four additional years of S -values, improving the baseline for many stars.

We are primarily focused on finding stellar activity cycles with periods between 2 and 25 yr, so we require 45 observations since 2005. Stars with fewer, often sporadically timed, observations are insufficient for robustly detecting activity cycles. We include stars with as few as five measurements for the average activity analysis. Out of the 710 stars in our sample, we search 285 for cycles, and the 425 additional stars are included in the summary activity analysis.

2.4. Data Validation and Rejection

To ensure the highest-quality data set, we start by adding S -values for non-iodine observations that were omitted from CLS1 because they do not contribute to the RV time series. The spectral segments used to calculate the S -values are shifted and scaled to a high signal-to-noise ratio (SNR) template of that same star (Isaacson & Fischer 2010). For 11 stars, no such template exists, so we use a spectrum of Vesta, a reflective spectrum of the Sun, that is shifted to observatory wavelength solution. Vesta spectra have the benefit of having the same format and blaze function as all other HIRES spectra. Those stars are HD 114762, HD 120136, HIP 60633, HD 152391, HD 10853, HD 6101, HD 112914, HD 167042, HD 73344, HD 177153, and HD 8375. S -values for these stars have the same quality and uncertainties as the others.

We make the following requirements at the level of individual observations for quality control:

1. S -values less than 0.10 are rejected as nonastrophysical. Fifty-six S -values are removed, and 98 are identified by eye as having poor extractions.
2. The SNR must be greater than 7 at continuum near 4000 Å, removing 276 S -values. One star, GL 406, has no observations that meet this threshold and is omitted throughout our analysis. See Bowens-Rubin et al. (2023) for a detailed analysis of this star.
3. The seeing must be less than 1''6 for C2 and B3 observations, excluding 1549 S -values from our sample.
4. Stars with $T_{\text{eff}} < 4000$ K are visually inspected and stars with Ca II H and K activity that extends beyond the 1.09 Å full width at half-maximum window that is used to calculate S -values are removed. Eight flare stars have flux emission in the H and K region that is not well modeled using S -values and are excluded. These stars also have a spectral helium line in emission that resides very near the H line, causing further ambiguity in the S -value measurement. The stars excluded are GL 83.1, GL 876, GL 905, HIP 112460, HIP 37766, HIP 5643, HIP 92403, and HD 75732B.
5. We retain 52,372 S -values from 2005 through 2023 October for 710 stars.

3. The 710-star Activity Sample

3.1. Overview

To assess the average activity of our sample we begin with the 710-star CLS1 sample that consists of slowly rotating FGK- and M-type stars that are amenable to RV measurements in search of exoplanets. Figure 3 presents our sample in the $\log(g)$ versus T_{eff} plane showing the average activity, ($\log R'_{\text{HK}}$), as a color scale. The sample is assembled to offer consistent sensitivity to long-period giant planets out to tens of astronomical units. The minimum baseline chosen of 8 yr, with 10 observations from HIRES and 20 total RVs, complements our search for stellar activity cycles, which tend to range from 2 to 25 yr (Baliunas et al. 1995; Baum et al. 2022). With many observations spanning the timescale of typical activity cycles, we present accurate measurements of the average activity for each star.

The California Legacy Survey (CLS) sample was originally selected to exclude stars that host known transiting planets and stars with known high metallicity. Samples of stars that focused on subgiants and young stars and those that had long-baseline observations due to the presence of hot Jupiters were also excluded. There are 178 known exoplanets or brown dwarfs around the stars in our sample.

3.2. Stellar Property Corrections

We amend the stellar property catalog from Rosenthal et al. (2021) by filling parameter values for five stars lacking T_{eff} . For HD 134439 and HD 134440, chemically peculiar twin stars in a binary system with a long-period orbit, we use the T_{eff} , $\log(g)$, $[\text{Fe}/\text{H}]$, and M_* from Chen et al. (2014). For HD 201092 and HIP 106924, we add the T_{eff} from our SpecMatch-Synthetic analysis of HIRES spectra (Petigura et al. 2017). We obtain the extremely low metallicity value of -2.5 for HIP 106924 from Joyce & Chaboyer (2018). For GL 528 B, we apply the SpecMatch-Empirical code to a HIRES spectrum (Yee et al. 2017). These are important additions since we are interested in the dependence of activity on T_{eff} .

3.3. Derived Properties

We calculate $\log(R'_{\text{HK}})$ (Noyes et al. 1984) and stellar age (Mamajek & Hillenbrand 2008) to examine activity correlations with fundamental and derived stellar properties and to check for correlations with activity cycle properties. Cincunegui et al. (2007), Suárez Mascareño et al. (2015), Astudillo-Defru et al. (2017), Mittag et al. (2013), and Marvin et al. (2023) each extend the $\log(R'_{\text{HK}})$ calibration to cool stars ($B - V = 1.6$) and $T_{\text{eff}} = 2700$ K. We use the Noyes et al. (1984) method to enable cross-referencing with other works, rather than the Marvin et al. (2023) method, which overestimates the color correction factor resulting in the overestimation of $\log(R'_{\text{HK}})$.

Since $B - V$ colors are used to calculate $\log(R'_{\text{HK}})$, we derive $B - V$ using the Ramírez & Meléndez (2005) method, which uses both T_{eff} and $[\text{Fe}/\text{H}]$ and is valid at T_{eff} of 7000–3870 K. For stars cooler than 3870 K, we use the CLS1 $B - V$ values. As a result, we use the Noyes et al. (1984) method for all of our analysis of $\log(R'_{\text{HK}})$ and derived stellar parameters. The use of consistent T_{eff} values when converting to $\log(R'_{\text{HK}})$ will be critical to our analysis of activity in relation to cycle period. With this choice, we urge caution when using $\log(R'_{\text{HK}})$ values for stars cooler than 3870 K due to the uncertainty in $B - V$.

3.4. The 710 Stellar Activity Analysis

Our stellar sample is presented in temperature versus surface gravity space in Figure 3 with a color scale indicating the stellar activity, $\log(R'_{\text{HK}})$. The prominently positioned subgiant stars that rise above the main sequence have the lowest stellar surface gravity values. Subgiant stars, with their larger stellar radii, typically have less stellar activity than main-sequence stars of the same T_{eff} . As they evolve and expand, their rotation rate slows to conserve angular momentum, and the decrease in density produces a more subdued stellar dynamo.

The zero-age main sequence is visible as active stars with high $\log(R'_{\text{HK}})$. Subdwarfs, with extremely low metallicities and old ages, fall below the zero-age main sequence. The coolest stars in our sample, below 4000 K, have a variety of activity values including the eight eruptive variables we exclude. This

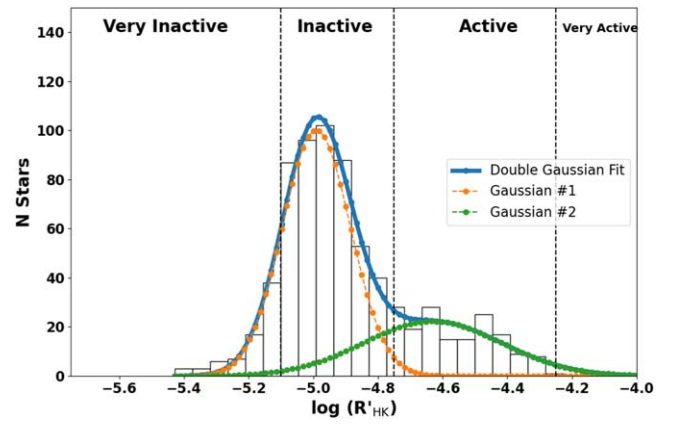


Figure 4. The distribution of our $\log(R'_{\text{HK}})$ data is modeled with a double Gaussian model with peaks at -5.001 and -4.886 . We find less structure than Gomes da Silva et al. (2021), perhaps due to the smaller number of stars in our survey compared to theirs. Activity qualifiers come from Wright et al. (2004). All 710 stars are included here.

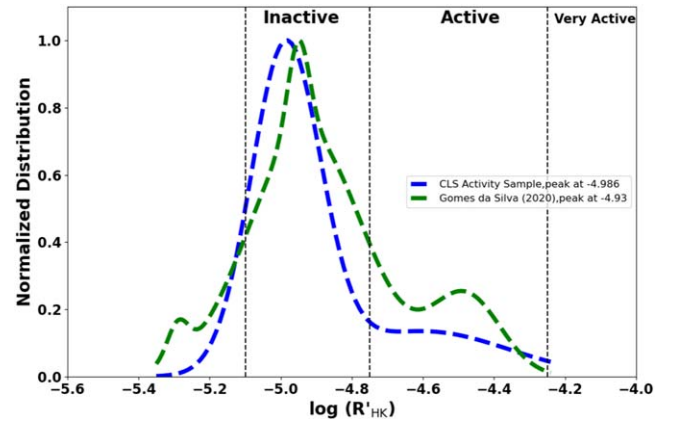


Figure 5. The distribution of our $\log(R'_{\text{HK}})$ data is modeled with a double Gaussian model and compared with that of Gomes da Silva et al. (2021), which had a T_{eff} lower limit of 4500 K. Our sample extends to T_{eff} of 3000 K so we omit stars cooler than 4500 K from this plot to make the comparison more direct. We see the two main peaks show up in both our sample and that of Gomes da Silva et al. (2021). Our main peak is slightly offset in the direction of less activity. Gomes da Silva et al. (2021) modeled four Gaussians compared to our two Gaussians, potentially causing this offset. The amplitude of the offset is 0.10, or twice the calibration offset for S -values from different instruments (Mittag et al. 2013). The astrophysical explanation is that CLS gave lower priority to more active stars.

may be due to the $\log(R'_{\text{HK}})$ metric being calibrated by Noyes et al. (1984) on Sunlike stars. Values of $\log(R'_{\text{HK}})$ are also sensitive to the choice of conversion from T_{eff} to $B - V$. Using the average of the stellar activity time series makes for a robust measurement of the average activity of our sample. Each of the stars in our sample has at least five observations.

We compare our sample to the primary Southern-sky planet search survey, the AMBRE-HARPS survey (Gomes da Silva et al. 2021), by modeling our distribution of $\log(R'_{\text{HK}})$ values as a sum of Gaussian contributions. Their catalog contains 1674 planet search stars, and they also focus on slowly rotating F-, G-, and K-type stars. Figure 4 shows our two-Gaussian fit to our 710-star sample and Figure 5 shows our sample compared to the AMBRE-HARPS sample. We normalize the y-axis and remove stars cooler than 4500 K in this plot to make as direct a comparison as possible. Their sample shows more structure

than ours, and peaks at a slightly more active value. Their small peak near -5.3 , attributed to giant stars, is not present in ours, due to our lack of giants. The additional structure for active stars may be due to their larger sample or is perhaps due to the CPS observing strategy of excluding active stars at early points in the survey. One possible systematic difference is the slit-fed versus fiber-fed spectrographs, HIRES and HARPS, respectively. However, we think this is sufficiently addressed in Section 2.1. The Gaussian properties representing our sample are available in Table 1.

We construct histograms for each of the FGK stars to compare the two samples as a function of spectral type (Figure 6). The smaller number of stars in our sample means that features in each distribution are not well defined, which leads to several degenerate model fits for each spectral type. Structurally the comparisons for each type of star are quite similar. The F stars have a broad distribution, represented by two Gaussians at $\log(R'_{\text{HK}})$ of -5.018 and -4.934 . The G-star distribution is dominated by a primary peak near -5.0 and a secondary peak of more active stars, at -4.50 , which is broad and low-amplitude. Our distribution of $\log(R'_{\text{HK}})$ for K stars is distinctly triple-peaked, similar to that in Gomes da Silva et al. (2021) but with a smaller peak at higher activity. Overall, we find the by-type comparison to be consistent with that found for planet search stars in the Southern Hemisphere.

3.5. Time-averaged Activity

We plot the S -value and $\log(R'_{\text{HK}})$ of the 710-star sample against fundamental stellar properties, highlighting, with different colors, the extreme ends of each stellar property distribution (Figure 7). Maroon data points represent stars with $T_{\text{eff}} < 4000$ K. Blue data points represent evolved stars, with $\log(g) < 4.0$. Low-metallicity stars with $[\text{Fe}/\text{H}] < -0.5$ are represented in green. Cyan symbols identify those stars with cycles identified in Section 4.

In panel (A) T_{eff} versus S -values are plotted and the familiar flat floor of activity from 6500 to 5000 K is visible, followed by a steady increase from 5000 to 4000 K (Isaacson & Fischer 2010; Mittag et al. 2013). The slope of the activity floor inverts down to our lowest- T_{eff} stars. There is a lower density of stars from 6000 to 5000 K that is elevated above the primary distribution of very inactive stars. The low-metallicity stars and low- $\log(g)$ stars fall near the S -value floor, as expected for older stars and subgiants. Panel (B), with $\log(R'_{\text{HK}})$ as a function of T_{eff} , shows that most stars in our sample are between 5000 and 600 K. The more active stars that lie above -4.8 may have cycles but are too variable to be strictly periodic.

Panel (C) plots the median S -value as a function of stellar surface gravity showing the low-gravity stars that have started to evolve off of the main sequence are at the floor of the S -value distribution. The highlighted very-low-metallicity stars mostly fall in a unique parameter space at a $\log(g)$ of 4.6–4.7. Although our metallicity distribution is sparse at $[\text{Fe}/\text{H}] < -0.5$ dex, the difference in S -value at that specific $\log(g)$ is distinct. The elevated population of stars at T_{eff} between 5000 and 6000 K in panel (A) is now compressed in panel (C) at a $\log(g)$ value of 4.5–4.7. This could be related to the age of these stars with younger stars being more active and having higher $\log(g)$. Panel (D) shows the most active stars have $\log(g)$ near 4.5, indicating that they are near the zero-age main sequence.

Panel (E) plots the median S -value for the 710 stars as a function of metallicity. At the bottom of the distribution, the subgiant population spans a wide range of $[\text{Fe}/\text{H}]$. Our sample is slightly overrepresented at $[\text{Fe}/\text{H}]$ greater than solar (45/55%), but is sufficiently populated from ± 0.4 such that we can draw conclusions about the presence of stellar activity cycles as a function of metallicity in Section 4.1. The Pearson correlation coefficients between the average S -value and metallicity and also between the S -value rms and metallicity are calculated and found to be less than 0.1 in each case. This suggests there is weak correlation between the spectroscopic activity metric S -value and metallicity, in contrast to photometric correlations to $[\text{Fe}/\text{H}]$ such as noted in Kepler flare stars (See et al. 2023). Our findings are consistent with Lovis et al. (2011), in which the $B - V$ to temperature conversion accounts for metallicity.

3.6. Activity Variability

The long time baseline over which these observations are collected and the multiple observations for each star lead to robust measures of the average activity of our sample. We examine the variability of S -value as a function of T_{eff} , $\log(g)$, and $[\text{Fe}/\text{H}]$ in Figure 8. Stars below 4000 K are the most variable, with significant variation due to the stellar rotation period variations. These stars are more heavily spotted, confusing our search for sinusoidal stellar activity cycles with periods on timescales of years. We adopt the values of T_{eff} , $\log(g)$, $[\text{Fe}/\text{H}]$, M_* , and R_* from Rosenthal et al. (2021), except where noted in Section 2.1. Table 2 contains the minimum, median, and maximum S -values, S -value rms value, standard deviation, $\log(R'_{\text{HK}})$, $\log(R'_{\text{HK}})$ rms, number of observations, and activity-derived stellar ages. The S -value time series are provided in Table 3.

4. The 285-star Sample to Search for Activity Cycles

We identify robust stellar activity cycles for use in analysis of stellar cycles as a function of stellar properties, including age. By requiring 45 observations, we define our stellar activity cycle sample of 285 stars. This choice helps to avoid a spurious detection of an activity cycle due to poor sampling.

4.1. Searching the 285-star Sample for Activity Cycles

The patterns of stellar activity can have complex structure on many different timescales, so we choose a simple sinusoidal model, with no eccentricity, to search for signals with periods between 2 and 25 yr. Cycles less than 2 yr are difficult to identify due to seasonal sampling, and ambiguity with rotation periods (Baliunas et al. 1995; Boro Saikia et al. 2018). We expect only the youngest (ages less than 1 Gyr) to have such short stellar activity cycles and the CPS RV planet surveys tend to exclude young stars in blind surveys. Notably, HD 115043 has a stellar activity cycle of 1.7 yr (Boro Saikia et al. 2018), but is not in our sample. HD 22049, ϵ Eri, has a multiple previously published cycle of 2.2 and 12 yr (Metcalfe et al. 2013) or perhaps a 3 yr, 11 yr, and 34 yr cycle (Fuhrmeister et al. 2023) when the calcium infrared triplet and X-ray measurements are analyzed. We have the sensitivity to detect these cycles with our data, but none of these periods pass our threshold. While the zero-eccentricity sinusoid model is sufficient for uniformly identifying activity cycles, a more complex model should be chosen for modeling young-star cycles and

Table 1
Gaussian Fit Parameters for the Activity Sample

Property Bin	Amplitude 1	Mean 1	Sigma 1	Amplitude 2	Mean 2	Sigma 2	Amplitude 3	Mean 3	Sigma 3	Chi-square	Reduced Chi-square
Full sample (710)	100.2	-4.990	0.1055	22.25	-4.632	0.2136	495	20.6
Comparison (564)	48.58	-4.985	0.097	6.81	-4.599	0.24	490	14.4
F-type stars (47)	7.757	-5.018	0.0508	2.764	-4.833	0.178	19.7	2.19
G-type stars (301)	35.98	-4.985	0.094	2.042	-4.483	0.272	280	11.7
K-type stars (171)	8.216	-4.950	0.068	4.617	-4.734	0.117	6.18	-4.443	0.044	190	6.13

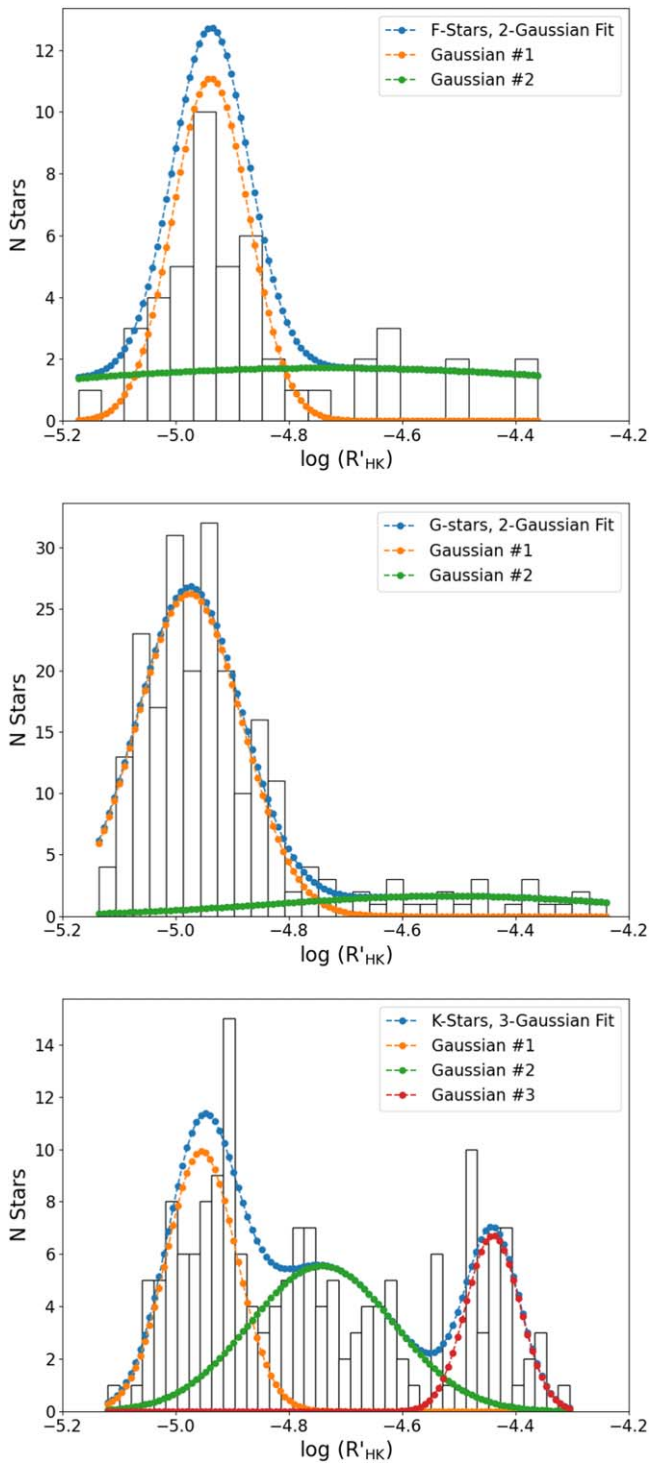


Figure 6. From top to bottom, the distributions of the $\log(R'_{\text{HK}})$ for the CLS sample are shown for F stars, G stars, and K stars, with $\log(g) > 4.2$. We model each distribution with a series of Gaussians and compare it to that in Gomes da Silva et al. (2021). Structurally the sample agrees with the AMBRE-HARPS sample of planet search stars from the Southern Hemisphere.

those with complex signals such as the cycles of HD 18803, HD 219134, HD 201092, and HD 140538A.

We utilize the Lomb–Scargle periodogram routine in *Astropy*²² and the “model normalization” option to identify

²² <https://docs.astropy.org/en/stable/timeseries/lombscargle.html>, *Astropy*’s Lomb–Scargle periodogram; see section on normalization = ‘model’.

peaks in the periodogram and fit a periodic function to the tallest peak. The “model-normalized” periodogram is a periodogram normalized around the residuals to the periodic model, rather than the constant model that is the default method of normalization. This normalization also accounts for the offset from zero typically expected from the generalized Lomb–Scargle periodogram. We limit the periodogram from 100 to 10,000 days (27.4 yr) and explore alternate limits such as 200–2000 days with no effect on recovered activity cycles. The strength of this method is the simplicity of the model, which is easy to parameterize and search. The weaknesses are that stellar activity cycles do not always stay in phase over many cycles, some cycles are better modeled by adding eccentricity, and stars with multiple cycles and different periods are difficult to identify.

We combine two quantitative metrics to identify stellar cycles. First, we calculate the difference between the standard deviation of the initial S -values and the standard deviation of the residuals, divided by the initial S -value standard deviation and the median S -value for that star (Equation (1)). Our threshold by this metric for detection is 1.20. We attempt to use chi-square as the best-fit metric but find the scatter in S -value over timescales of weeks and months makes this metric less useful. We determine the threshold value by ranking our stars with this metric and finding where the cycles become unreliable by eye.

$$\text{Threshold} = \frac{(\text{STD}_f - \text{STD}_i)}{\text{STD}_i * \text{Median}(S\text{-value})}. \quad (1)$$

As a secondary metric, we identify cycles through the Lomb–Scargle periodogram as those having a peak greater than 0.5. The maximum peak of any star is 14.0 (HD 192310) and the median peak value for all detected cycles is 2.01. The weakest signal in our data is from GL 699, with a peak value of 0.501. We also remove stars with candidate cycles if the second peak in the periodogram is more than 75% of the primary peak. Such peaks indicate that the identified period is not sufficiently unique for our purposes. Using the ratio of the first and second tallest peaks eliminates many stars that have very plausible cycles but have ambiguous periods. Many stars with cycles much longer than our observing baseline are removed in this quality cut. With the periodogram qualification, we recover 27 cycles that do not pass our threshold from Equation (1), including all of the detected cycles in stars below T_{eff} of 4400 K. By including our reliability metrics for all 285 stars, future studies can choose different thresholds to fit their analysis needs.

For three stars, we remove a linear trend and afterward detect an activity cycle. These trends are indicative of a second cycle, as has been studied most recently by Mittag et al. (2023). Those stars are HD 219134, HD 158633, and HD 82943. When a trend is removed for HD 23356 and HD 201092, they show candidate cycles but do not pass the quantitative thresholds. Generally, our search method is insensitive to cycles longer than our baseline of 20 yr and fails to robustly identify any previously unknown secondary cycles.

These combined metrics detect stars with incredibly small overall variations such as HD 126614 with a peak-to-peak S -value amplitude fit value of 0.0041. For comparison, HD 10700, considered an activity standard, has an S -value standard deviation of 0.0012 and a relative dispersion of 0.8%. The least active stars with and without cycles are discussed in

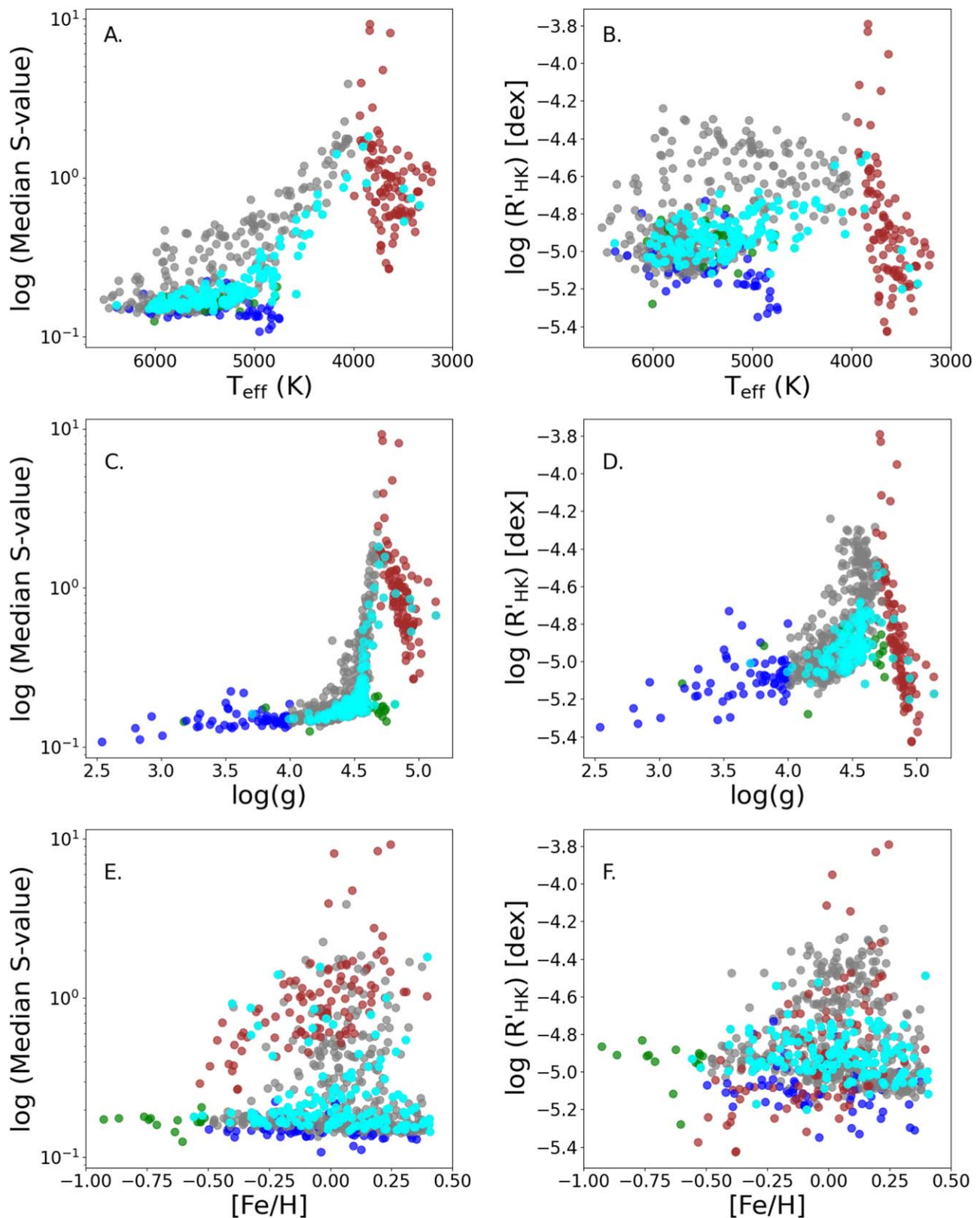


Figure 7. The values of T_{eff} (panels (A) and (B)), stellar surface gravity (panels (C) and (D)), and $[\text{Fe}/\text{H}]$ (panels (E) and (F)) are plotted vs. the S -value and $\log(R'_{\text{HK}})$ for the 710 stars. Maroon data points represent cool stars, with $T_{\text{eff}} < 4000$ K. Blue data points are stars with $\log(g) < 4.0$, i.e., subgiants, and green data points represent stars with metallicity less than -0.5 . Cyan symbols identify stars with cycles. The bottom two panels exclude 11 stars with $[\text{Fe}/\text{H}] < -1$. Gray data points represent stars not in the extremes of T_{eff} , $\log(g)$, and $[\text{Fe}/\text{H}]$ and without cycles.

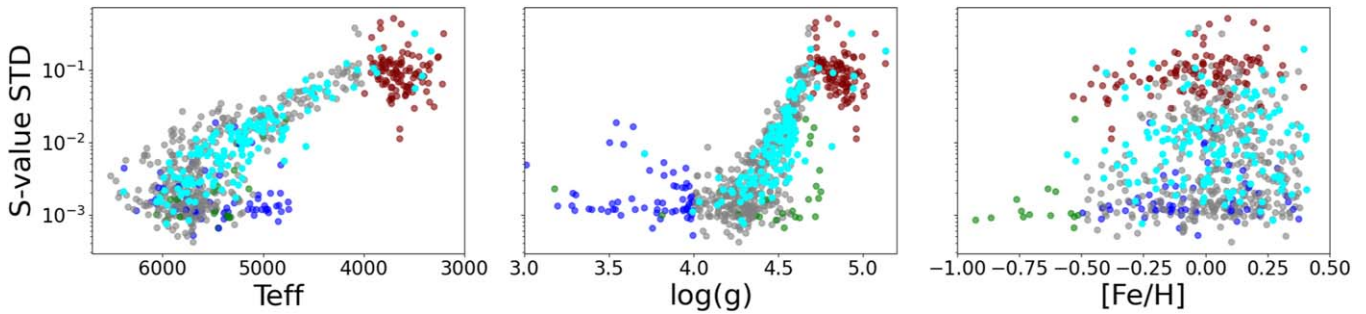


Figure 8. The S -value standard deviation is plotted as a function of T_{eff} , $\log(g)$, and $[\text{Fe}/\text{H}]$ for all 710 stars in our full sample. Stars with low $\log(g)$ are in blue, and stars with $T_{\text{eff}} < 4000$ K are in maroon. The lowest-metallicity stars are shown in green. Eleven very-low-metallicity stars are taken off the plot. Cyan marks stars with detected cycles. The dichotomy of stars with low $\log(g)$ values is intriguing. We do not sample all of the parameter space equally, but the marked cycles still identify the area most likely to contain periodically cycling stars. The gray data points represent stars with $T_{\text{eff}} > 4000$ K, $\log g > 4.0$, and $[\text{Fe}/\text{H}] > -0.5$ and include stars above and below our threshold of 45 observations.

Table 2
Average Activity Values

Star	S_{min}	S_{max}	S_{med}	S_{STD}	N_{obs}	$B - V$	Rphk_Noyes	Age (Gyr)
HD 10002	0.1585	0.1668	0.1598	0.00205	44	0.804	-5.041	6.45
HD 10008	0.3886	0.4526	0.4238	0.01347	37	0.768	-4.414	0.46
HD 100180	0.1615	0.1794	0.1679	0.00325	63	0.564	-4.916	4.12
HD 100623	0.1751	0.2165	0.1913	0.00930	82	0.763	-4.890	3.74
HD 101259	0.1392	0.1467	0.1443	0.00227	13	0.739	-5.118	8.37
HD 10145	0.1679	0.1769	0.1724	0.00150	27	0.660	-4.929	4.32
HD 101501	0.2769	0.3719	0.3135	0.02552	15	0.701	-4.526	0.99
HD 102158	0.1585	0.1601	0.1598	0.00050	12	0.557	-4.965	4.93
HD 103095	0.1910	0.2271	0.2087	0.00960	17	0.665	-4.774	2.44
HD 103432	0.2372	0.2716	0.2571	0.01037	9	0.645	-4.614	1.40

(This table is available in its entirety in machine-readable form in the [online article](#).)

Table 3
Chromospheric Time Series

Star	Filename	BJD	S -value	SNR	Decker	Seeing (arcsec)
HD 185144	bj01.46	13237.736	0.2112	55	B5	1.0
HD 185144	bj01.47	13237.738	0.2120	34	B5	1.1
HD 185144	bj01.48	13237.739	0.2094	28	B5	1.1
HD 185144	bj01.49	13237.740	0.2118	30	B5	1.2
HD 185144	bj01.50	13237.740	0.2094	36	B5	1.0
HD 185144	bj01.51	13237.741	0.2112	43	B5	1.1
HD 185144	bj01.52	13237.742	0.2113	43	B5	1.0
HD 185144	bj01.53	13237.742	0.2114	48	B5	1.1
HD 185144	bj01.54	13237.743	0.2101	52	B5	1.0
HD 185144	bj01.55	13237.744	0.2115	49	B5	1.0

(This table is available in its entirety in machine-readable form in the [online article](#).)

Section 5.6. From the 285 stars searched, we present 138 stellar activity cycles and next discuss our recovery of previously known cycling stars.

4.2. Cycle Comparison to Previous Studies

4.2.1. Mount Wilson Cycles

Most published activity cycles that were produced with S -values have been collected by the Mount Wilson Observatory HK Project. Baliunas et al. (1995) found that 52/111 main-sequence stars have cycles. The regularity of stellar cycles is dependent on age: young stars rarely display a smooth, cyclic variation; intermediate-age stars have occasional smooth cycles; and stars as old as the Sun have smooth

cycles (Baliunas et al. 1995). Although our sample is vastly different, we find 138/284 stars have cycles. Our sinusoidal search is not sensitive to nonperiodic cycles of young stars such as HD 22049. Our search is most sensitive to the regular cycles of stars older than 1 Gyr. The largest sample of Mount Wilson stars compiled has 335 stars. From our 710-star sample, 173 stars overlap and we independently identify 44 cycles from those 173 stars. Since our sample contains a broader range of stellar types, we are exploring parameter space beyond Baliunas et al. (1995) allowing for the examination of correlations between cycle periods and stellar properties.

Summary analysis of the Mount Wilson cycles has claimed that the Sun is near the upper mass limit for cycling stars

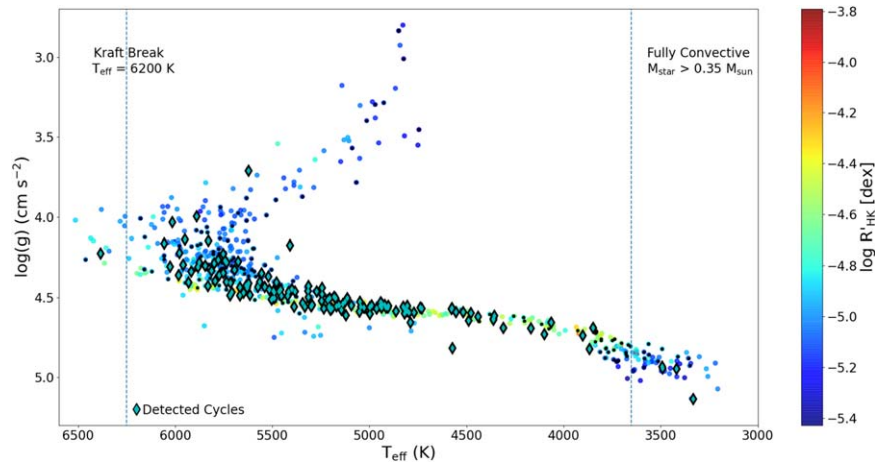


Figure 9. Effective temperature, stellar surface gravity, and median $\log(R'_{\text{HK}})$ value for the 710 stars in our sample. Diamonds show detections of 138 stellar activity cycles. Circles identify the 285 stars with more than 45 observations that are searched for cycles, and the color scale represents $\log(R'_{\text{HK}})$.

(Schröder et al. 2013), but the identification of many cycles down to 4400 K presented here and the handful of M dwarfs found here and by Irving et al. (2023) show that stars across the main sequence can be in cycling states.

4.2.2. Studies of Keck Data

We cross-check the 13 cycles from 59 stars examined in Baum et al. (2022), adding two years of HIRES data, and find 10 of the 13 cycles. Of those not detected, HD 166620 is in the well-studied minimum phase of its cycle (Luhn et al. 2022), while HD 101501 and HD 152391 have fewer than 45 observations. For the cycles that we expect to detect, our algorithm identifies them.

The CLS activity time series has been analyzed in relation to precise RVs. In CLS1, Table 7 mentions 43 false-positive planet signals that are attributed to stellar activity cycles, and 13 false positives due to rotation periods. We confirm 41 of the 43 as stellar activity cycles. Luhn et al. (2020) listed stars with possible stellar activity cycles, but the focus of that work was on average activity and its impacts on RV precision. For their stars that overlap with our sample, we quantify the intensity and period of those signals.

4.2.3. Johnson et al. (2016)

Johnson et al. (2016) used data collected from 295 spectra from the 2.7 m Harlan J. Smith Telescope at McDonald Observatory from 1998 to 2015 to monitor the RV of the HD 219134 system and also collected S -value measurements of stellar activity. They detected a stellar activity cycle of 11.7 yr with no linear trend. Our analysis finds a cycle period of 13.4 yr after removing a robust linear trend over the observation baseline of 20 yr. The discrepancy in the detection of a linear trend may be explained by differing measurement uncertainties and is worthy of further exploration.

4.2.4. Toledo-Adrón et al. (2019)

Toledo-Adrón et al. (2019) studied the stellar activity of GL 699, Barnard’s star, and revealed an activity period of 8.8 yr in the Ca II H and K S -values. Our measured cycle of 8.5 yr is consistent with their value. Toledo-Adrón et al. (2019) also used photometry to determine the activity cycle finding a 10.5 yr cycle. Their conclusion that GL 699 is a very inactive

star is consistent with our finding of the periodogram amplitude being just above the threshold of detection.

4.2.5. Mittag et al. (2023)

Mittag et al. (2023) listed 34 chromospherically detected activity cycles around FGK stars. For the 15 stars that overlap with our sample, and have more than 45 observations, we recover 14 of the cycles. HD 201092 has two cycles, but neither passes our thresholds. The 11 yr period is not detected due to our choice to fit only circular periodicity. Future studies that include the Mount Wilson and Keck/HIRES data sets can potentially confirm these complex cycles. Future analyses may require different levels of confidence in the cycle detection or will be conducted with a different model.

4.2.6. Studies of Fully Convective Stars

Photometric data from the ASAS-SN project identified 13 of 15 fully convective M dwarfs showing stellar cycles (Irving et al. 2023). Among overlapping stars in our sample with 45 observations HIP 80824 (GJ 628) and HIP 109388 (GJ 849) are not detected. GJ 317 has two cycles, but we detect neither. HIP 103039 (LP 816-60), HIP 57548 (GJ 447), GJ 285, GJ 54.1, GJ 234, and GL 406 all have fewer than 45 Keck/HIRES observations, falling below the inclusion threshold. The cycles with periods of a few years that Irving et al. (2023) detected with photometry must not have periodic signals amenable to detection with the Ca II H and K emission lines. The lack of chromospheric confirmation of the photometric cycles may be due to complex structures to which our simple sinusoid model is not sensitive. Indeed other studies have identified chromospheric cycles in M dwarfs (Suárez Mascareño et al. 2016; Wargelin et al. 2017).

From this point on we turn our focus to the 285 stars that have at least 45 Keck/HIRES S -values since 2005, eventually narrowing down the parameter space to show that nearly every star in that range has a periodic activity cycle.

5. Stars with Cycles

We examine the population of stars with identified cycles, starting within the context of fundamental stellar properties. Stars with cycles span a range of temperatures ($6385 \text{ K} > T_{\text{eff}} > 3332 \text{ K}$), stellar surface gravities ($5.13 > \log(g) > 3.71$),

and metallicities ($-1.61 < [\text{Fe}/\text{H}] < 0.41$). The second lowest metallicity is -0.56 . Figure 9, similar to Figure 3, identifies stars that are searched and those with stellar cycles in the T_{eff} versus $\log(g)$ parameter space. Most cycling stars are in the main sequence with temperatures from 4700 to 5900 K. Metallicity does not appear to hold a pivotal role in the presence of chromospherically detected activity cycles (see Section 5.4). Stars with detected cycles are listed in Table 4 along with their cycle properties.

In the following section, we divide stars below 4700 K from those with higher T_{eff} . This divide exists for two reasons. Near 4700 K, the models used to determine fundamental stellar parameters change due to the underlying physics inside stars. For example, stars below this divide use SpecMatch-Empirical (Yee et al. 2017) and stars above use SpecMatch-Synthetic (Petigura et al. 2017). The second reason is the historical division of stars at this T_{eff} , for which rotation periods and convective turnover times were devised (Noyes et al. 1984).

Figure 10 shows histograms of the fundamental stellar parameters T_{eff} , $\log(g)$, and $[\text{Fe}/\text{H}]$ as well as the derived parameters R_* , M_* , and $\log(R'_{\text{HK}})$. Gray identifies the 710-star sample, yellow represents the 285-star sample that we search for cycles, and cyan represents detected cycles.

Figures 11 and 12 show the amplitudes and periods of the detected cycles as a function of both fundamental and derived stellar properties. In terms of amplitude, stellar cycles tend to increase as T_{eff} decreases and main-sequence stars have larger amplitudes than evolved stars, but some main-sequence star cycle amplitudes are comparable to those of subgiant stars. We find no correlation between metallicity and cycle amplitude or cycle period. A quantitative analysis is detailed in Section 5.4. We explore an intriguing correlation of cycle period to T_{eff} for the activity range within $\log(R'_{\text{HK}})$ of -4.7 to -4.9 in Section 6.

5.1. Solar-type Stars with Cycles

Previous surveys of chromospheric activity have focused on solar-like stars identified with similar $B - V$ colors and bolometric luminosities to the Sun (Baliunas et al. 1995; Henry et al. 1996), and we define our solar-similar sample to have $5600 \text{ K} < T_{\text{eff}} < 5900 \text{ K}$, with no metallicity or $\log(g)$ restrictions. Out of 70 solar-like stars, we find 29 stars with cycles having periods between 3.9 and 23 yr. This subsample is evenly distributed in metallicity (± 0.3 dex) and $\log(R'_{\text{HK}})$ (-4.8 to -5.08). When the average activity is used to derive the rotation period and age (Mamajek & Hillenbrand 2008), the solar-similar sample ranges from 14 to 34 days and from 2.7 to 7.4 Gyr, respectively. The range of cycle periods for this subsample offers insight into the decreasing activity and rotation as a function of age for solar-type stars. The cycle periods of solar-type stars and their dependencies on stellar properties are highlighted as yellow crosses in Figures 11 and 12.

5.2. Short-period Cycles

We identify 45 cycling stars with periods less than 7 yr. Baliunas et al. (1995) found that stars with cycles of periods shorter than 7 yr have a higher false-alarm probability, marking them as “fair” or “poor.” We use numeric thresholds that can be used to mark the robustness of a detection but find the vastly different sampling can require judgment calls when defining thresholds. HD 218868 is an example of a convincing cycle with a period of just 4.8 yr. Since the Mount Wilson survey had

Table 4
Detected Stellar Cycles for 138 Stars

Star	Amplitude _{fit}	Period _{fit}	Threshold	Peak 1	Peak 2
HD 100180	0.1704	3.33	1.76	1.01	0.36
HD 100623	0.2070	8.03	2.57	2.88	0.70
HD 103932	0.5085	9.00	1.36	5.49	0.47
HD 104304	0.1643	10.00	2.63	1.96	0.44
HD 10476	0.1977	9.11	1.39	0.86	0.26
HD 107148	0.1607	5.69	2.20	1.32	0.57
HD 109358	0.1674	13.50	1.87	1.09	0.36
HD 110315	0.3774	11.81	1.96	6.39	0.64
HD 111031	0.1496	13.72	1.29	0.53	0.28
HD 114783	0.2055	9.10	2.25	2.01	0.29
HD 116442	0.1686	18.09	2.49	1.84	0.21
HD 116443	0.1880	14.24	2.57	2.25	0.25
HD 122064	0.2863	12.81	2.91	11.62	1.06
HD 122120	0.6042	20.86	0.66	1.71	0.52
HD 125455	0.1946	9.87	3.39	5.65	0.57
HD 126053	0.1660	17.53	1.82	1.04	0.34
HD 126614	0.1469	16.15	2.24	1.19	0.45
HD 127334	0.1521	16.08	1.52	0.68	0.42
HD 130992	0.3386	3.11	0.71	0.69	0.42
HD 136713	0.3320	6.85	1.10	1.30	0.36
HD 139323	0.2467	8.84	2.28	2.57	0.23
HD 140538A	0.2061	3.96	1.81	1.43	0.29
HD 14412	0.2032	6.15	2.51	2.68	0.63
HD 144287	0.1673	19.29	3.54	4.31	0.56
HD 145675	0.1883	11.20	3.49	4.24	0.21
HD 145958A	0.1916	7.63	2.27	1.75	0.59
HD 145958B	0.1868	8.30	1.79	1.15	0.75
HD 1461	0.1632	14.10	1.93	1.09	0.12
HD 146233	0.1735	6.27	3.30	3.87	0.97
HD 148467	0.7626	4.03	0.46	1.12	0.83
HD 149806	0.2244	6.71	2.08	1.99	0.95
HD 154088	0.1634	15.20	3.80	4.92	1.65
HD 154345	0.2320	6.95	2.82	5.58	0.40
HD 154363	0.5312	9.53	1.38	5.18	0.72
HD 155712	0.2296	9.33	3.15	5.12	0.85
HD 156279	0.1783	12.50	2.19	1.63	0.37
HD 156668	0.2462	11.38	1.95	2.37	0.19
HD 156985	0.3036	7.82	2.34	5.90	0.42
HD 158633	0.1780	11.83	2.13	1.51	0.90
HD 159062	0.1738	16.85	2.68	2.38	0.55
HD 16160	0.2371	12.43	2.31	3.40	0.48
HD 168009	0.1616	17.52	1.79	0.96	0.47
HD 170493	0.4691	8.75	1.26	3.33	0.98
HD 172051	0.1719	8.36	2.08	1.35	0.55
HD 17230	0.8034	15.20	0.24	0.53	0.13
HD 18143	0.1801	13.67	2.98	2.91	0.40
HD 182488	0.1704	11.54	2.79	2.34	0.35
HD 183263	0.1576	7.00	2.85	2.07	0.19
HD 185144	0.2179	5.93	1.94	1.78	0.20
HD 186408	0.1534	20.20	1.68	0.79	0.25
HD 18803	0.1894	5.04	2.20	1.75	0.31
HD 190406	0.1919	15.02	1.21	0.64	0.47
HD 191408	0.1978	16.77	2.56	2.56	0.76
HD 192310	0.2171	10.67	4.12	14.26	0.94
HD 19308	0.1627	22.28	3.11	2.86	0.40
HD 196761	0.1785	11.40	3.79	7.29	1.63
HD 197076	0.1886	5.31	3.17	4.27	2.33
HD 199305	1.6523	6.30	0.24	1.61	1.11
HD 201091	0.6256	7.17	0.68	1.75	0.38
HD 20165	0.2289	7.78	3.03	6.05	0.76
HD 202751	0.2474	12.49	3.03	6.29	0.52
HD 20619	0.2023	4.42	2.43	2.63	0.58
HD 208313	0.3012	5.96	1.80	2.57	0.68
HD 209458	0.1616	4.79	1.96	1.13	0.73
HD 210302	0.1609	5.85	1.65	0.83	0.55

Table 4
(Continued)

Star	Amplitude _{fit}	Period _{fit}	Threshold	Peak 1	Peak 2
HD 213042	0.4273	8.01	1.34	2.97	1.23
HD 215152	0.2642	8.04	1.71	2.03	0.62
HD 216259	0.1938	15.96	3.62	7.17	0.88
HD 216520	0.2015	19.19	2.25	2.11	0.48
HD 218566	0.2967	9.66	2.66	6.10	0.31
HD 218868	0.2133	4.84	2.43	2.78	0.40
HD 219134	0.2758	13.27	2.25	4.33	0.33
HD 219538	0.2516	7.09	1.88	2.24	1.26
HD 219834B	0.2059	9.70	3.61	6.77	0.77
HD 220339	0.2675	5.87	2.17	3.03	1.25
HD 221354	0.1599	18.84	1.51	0.71	0.19
HD 224619	0.1702	18.06	2.57	1.99	1.04
HD 239960	1.4673	15.78	0.32	0.88	0.49
HD 24496	0.2008	5.86	2.87	3.27	0.58
HD 25329	0.1952	6.01	2.36	2.16	0.33
HD 25665	0.3042	6.52	1.68	2.47	0.53
HD 26151	0.2061	16.35	3.24	5.25	0.40
HD 26161	0.1531	20.12	1.79	0.87	0.37
HD 26965	0.2060	9.11	2.13	1.92	0.42
HD 28005	0.1633	13.79	2.80	2.28	0.68
HD 28946	0.2443	5.90	2.38	3.29	1.49
HD 29883	0.1958	14.00	3.48	6.49	0.42
HD 31253	0.1526	13.08	1.48	0.66	0.43
HD 32147	0.2933	9.53	0.93	0.74	0.26
HD 34445	0.1665	23.01	1.69	0.91	0.23
HD 36003	0.4252	10.98	1.44	3.64	0.72
HD 36395	2.0485	2.30	0.21	1.63	1.22
HD 3651	0.1788	10.01	3.14	3.38	0.35
HD 37008	0.1821	21.27	1.37	0.76	0.27
HD 3765	0.2186	12.80	3.18	5.96	0.31
HD 38230	0.1642	23.15	2.32	1.54	0.81
HD 38529	0.1734	5.46	2.63	2.02	0.54
HD 4256	0.2639	9.66	1.73	1.93	0.32
HD 42618	0.1639	10.16	2.83	2.30	0.19
HD 43947	0.1586	12.88	2.12	1.26	0.52
HD 4628	0.2173	7.91	2.73	3.46	0.81
HD 4747	0.2676	4.90	1.43	1.41	0.65
HD 4915	0.2046	4.86	1.72	1.19	0.42
HD 49674	0.1977	4.05	1.12	0.62	0.36
HD 50499	0.1516	3.69	2.51	1.56	0.76
HD 51419	0.1948	23.43	2.09	1.67	0.23
HD 51866	0.3395	7.17	0.98	1.10	0.30
HD 52711	0.1602	13.96	2.91	2.42	0.49
HD 62613	0.2089	5.75	3.27	5.28	0.90
HD 65277	0.2543	12.19	2.66	6.53	0.51
HD 68988	0.1630	5.29	2.67	1.99	0.62
HD 69830	0.1734	10.83	1.84	1.12	0.60
HD 72673	0.1866	10.47	4.03	9.65	1.67
HD 73667	0.1717	19.00	2.33	1.64	0.59
HD 74156	0.1476	16.01	2.05	1.05	0.19
HD 75732	0.1973	11.02	3.79	6.74	0.27
HD 7924	0.2285	7.49	2.40	3.15	0.27
HD 80606	0.1566	16.27	1.96	1.06	0.34
HD 82943	0.1716	2.96	1.56	0.84	0.28
HD 8389	0.2158	10.67	3.24	4.31	0.42
HD 84035	0.5291	8.03	0.95	2.16	0.73
HD 87359	0.2047	4.40	1.91	1.64	0.82
HD 87883	0.2780	7.83	1.85	2.93	0.52
HD 89269	0.1698	16.95	2.84	2.63	0.37
HD 90875	0.7309	18.71	0.84	2.38	0.62
HD 9562	0.1509	15.39	1.57	0.71	0.29
HD 97658	0.2074	9.01	3.64	8.63	0.30
HD 98281	0.1801	15.51	2.53	2.33	0.94
HD 99491	0.2128	6.15	2.61	3.26	0.33
HD 99492	0.2820	9.81	1.97	2.81	0.19

Table 4
(Continued)

Star	Amplitude _{fit}	Period _{fit}	Threshold	Peak 1	Peak 2
HD 9986	0.1794	5.03	1.87	1.23	0.68
GL 239	1.0562	15.24	0.38	1.39	0.86
GL 273	0.8215	2.94	0.30	0.66	0.33
GL 699	0.8470	8.48	0.27	0.50	0.31
HIP 19165	0.7498	5.68	0.43	0.94	0.69
HIP 41689	0.9481	3.03	0.23	0.56	0.38
HIP 74995	0.5778	3.80	0.38	0.58	0.17
S130811	1.1601	13.58	0.45	2.27	0.43

(This table is available in machine-readable form in the [online article](#).)

sufficient sampling and sensitivity for detecting short-period cycles, their sample selection is likely responsible for non-detections. Younger stars (ages less than 1 Gyr), such as HD 22046, have previously identified cycles, but we intriguingly find 15 stars near solar temperature with periods less than 7 yr (Section 6).

5.3. Studies of Fully Convective Stars

As with fully radiative stars, stars with masses below $0.35 M_{\odot}$ become fully convective and lose their tachocline, requiring a different mechanism for generating magnetic fields compared to solar-type stars (Irving et al. 2023). Four fully convective (T_{eff} less than 3500 K) stars have periodic activity that passes our thresholds (Section 4.1): HD 239960, GL 273, GL 699, and HIP 74995. HD 239960 has observations during a flare that are much higher than the average activity value. We include flare stars—except those with helium emission that were omitted in Section 2.1—and less active stars that we can measure with traditional S -values.

HD 95735 has a candidate cycle showing a downward linear trend, indicating a period beyond our baseline of observations. For fully convective stars that are amenable to the S -value measurement, we find that the S -values are sometimes dominated by the rotation period, so our exclusion in our periodogram search below 100 days is useful. The cycles in fully convective stars are identified with the periodogram peak method, and are not typically identified with the threshold described by Equation (1).

The stellar activity of GL 699 was studied by Lubin et al. (2021), but that study focused on periods less than 1000 days. The peak value in the GL 699 periodogram is very close to our acceptable threshold, and combining multiple data sets would provide more confidence in the detection. A comparison between our results for GL 699 and those of Toledo-Padrón et al. (2019) is summarized in Section 4.2.4.

5.4. Metallicity of Stars with Cycles

We find no correlation between cycle period or amplitude and stellar metallicity. First, we divide the stars searched into those with supersolar and those with subsolar metallicity, and we find similar ratios of stars searched (45%/55%) to cycles found (44%/56%). The evidence for a correlation of the flare rate of Kepler stars with the metallicity found in Kepler stars (See et al. 2023) does not hold for our sample. Our sample

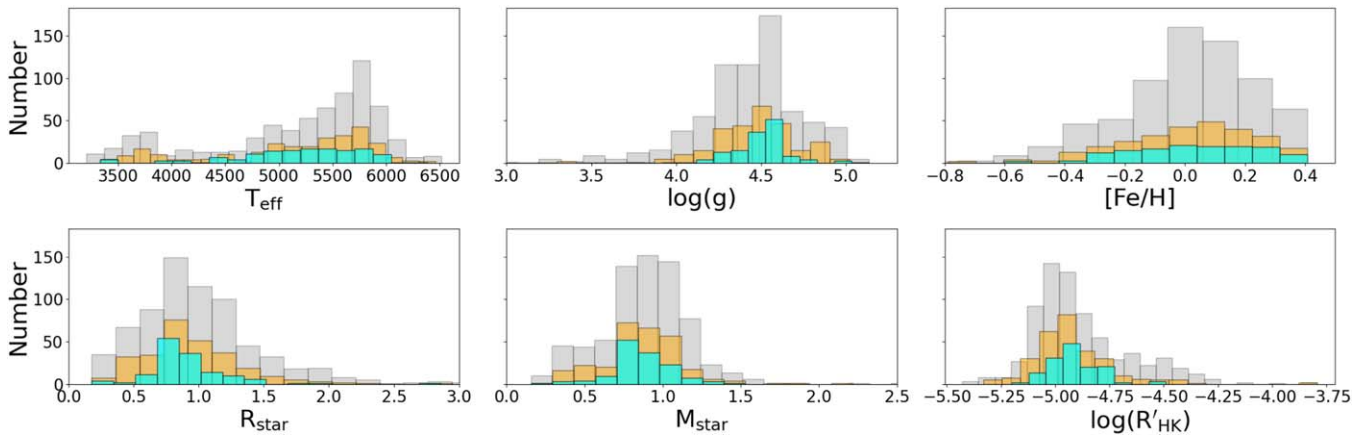


Figure 10. Distributions of T_{eff} , $\log(g)$, $[\text{Fe}/\text{H}]$, R_{star} , M_{star} , and $\log(R'_{\text{HK}})$ for the 710 stars in our sample. The yellow areas show the 256 stars that have more than 45 observations, and cyan identifies the 138 stars with a cycle from this work. The stellar parameters of the stars that are searched and those that have cycles are representative of the entire sample, and are not strictly confined to particular stellar properties. Twenty-eight stars have radii larger than 2.5.

avoids stars with flares, which tend to be more active, making a direct comparison with studies of flare stars difficult.

The most metal-poor star with a detected cycle, HD 25329, has an $[\text{Fe}/\text{H}]$ of -1.61 . It has a smaller cycle amplitude compared to stars with a similar T_{eff} by a factor of 3. The extremely low metallicity is unusual in our sample, and the CLS1 stellar parameters list the Gaia parallax as an unlikely $12''$, so the T_{eff} may not need to be revisited. It is also the outlier in panel (B) of Figure 11, raising suspicion.

To quantify the correlation between metallicity and activity, we calculate the Pearson and Spearman correlation coefficients for metallicity and a variety of activity indicators, finding no strong correlations. For correlations between $[\text{Fe}/\text{H}]$ and cycle period and between $[\text{Fe}/\text{H}]$ and cycle amplitude, we find coefficients below 0.10 indicating there is little or no correlation between metallicity and either cycle period or cycle amplitude.

5.5. Stars with Multiple Periodic Cycles

Our time baselines are sufficient to identify stars that have multiple simultaneous cycles, but our search method does not recover any of the known occurrences. HD 22049 (Metcalfe et al. 2013; 2.95 ± 0.03 yr and 12.7 ± 0.3 yr), HD 32147, HD 4915, HD 219234 (trend), HD 4628 (trend), and HD 45184 (5.14 yr; Flores et al. 2016) all show evidence of a second cycle. HD 100180 shows two possible periods in Oláh et al. (2016) but we only find one, and Baum et al. (2022) found none. HD 201091 and HD 201092 both have two cycles that will be apparent when combining the Mount Wilson data. HD 18803 has one strong cycle that changes significantly in amplitude over 20 yr. HD 219834B shows a linear trend on top of a cycle, indicative of a second cycle. The shorter of the cycles is typically not represented well by a sinusoid, so our nondetections are limited by our search method not our data quality.

5.6. The Least Active Stars

The search for stars in a Maunder minimum, or magnetic minimum state, attempts to connect the Sun’s activity cycles to the cycles of other stars. HD 4915 is a candidate star in a Maunder minimum-like state (Shah et al. 2018), but our extended time baseline shows two cycles. One periodicity is at

4.9 yr, and the second is more than 40 yr, and the longer-period cycle is now turning higher. We detect the 4.9 yr period but cannot limit the period of the second cycle with Keck data alone. HD 166620 is the most convincing to have strong evidence in favor of being a Maunder minimum-like star (Baum et al. 2022; Luhn et al. 2022), and it continues to show very low variation in our extended time series.

In Isaacson & Fischer (2010), the 1% dispersion in the S -values of HD 10700 was used to gauge the systematic uncertainty of the S -values. Gomes da Silva et al. (2021) found a dispersion of 0.83%, which is comparable to our extended time baseline for HD 10700 S -values 0.75% ($0.00125/0.1674$). Our least active star with more than 45 observations is HD 55575 with a relative dispersion of $0.0007/0.1562 = 0.45\%$. Fifty stars have a smaller S -value standard deviation than HD 10700 and should be considered the least active well-sampled (45 observations or more) stars in our sample (Table 2). Differentiating inactivity due to stellar evolution, stellar viewing angle, and main-sequence spindown would be an interesting extension of this work.

5.7. Unexpectedly Cycling Stars

For stars with stellar surface gravity less than 4.0, we find that out of 28 stars only HD 38529 ($\log(g) = 3.93$) has a detectable cycle, and its period is 6.11 yr. Baliunas et al. (1995) stated that “the range of masses that can support solar-like magnetic activity is imprecisely known,” and although we expect stars to lose their cycles as they age, spin down, and evolve, this cycle is an unexpected robust detection. HD 38529 has two substellar companions; the more massive of the two has an $M_{\text{ini}} = 13.2 M_{\text{Jup}}$, $P = 5.8$ yr, and eccentricity = 0.35. Our periodogram analysis shows that the peak in both the RV and the S -value periodogram is at 5.8 yr. This system is worthy of an analysis that explores the relationship between the planet and the activity cycle of this post-main-sequence star with stellar radius of $2.8 R_{\odot}$ and a robust activity cycle. Gravitational interactions between exoplanets and stars have not been found to cause activity cycles (Obridko et al. 2022), but main-sequence stars (including our own) have been found to have activity cycles and planets with similar periods (Wright 2016).

Fully radiative stars, above the Kraft break (Kraft 1967), lack the radiative-convective boundary that is known to generate magnetic fields. Without a tachocline, it is not clear what

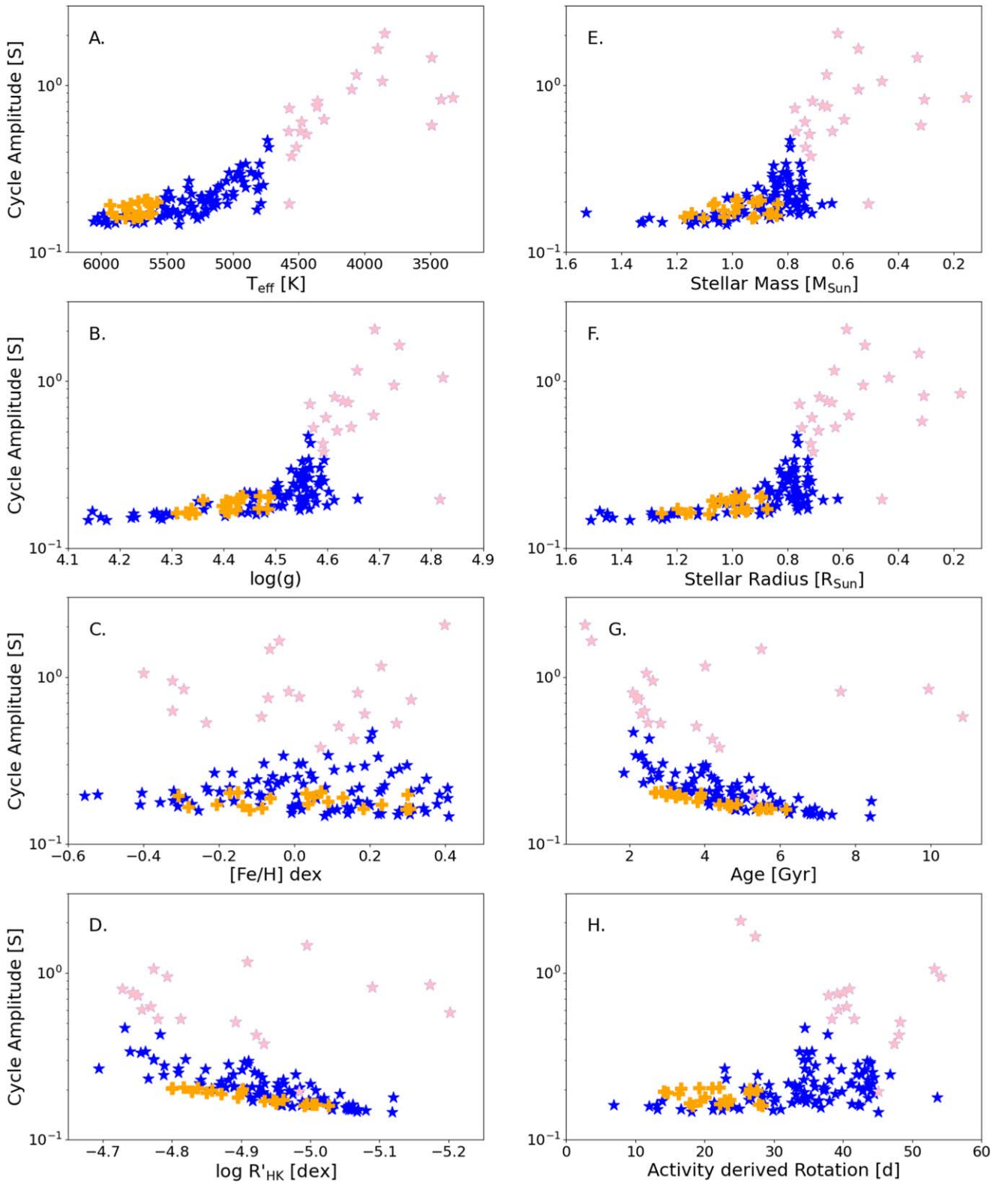


Figure 11. Stars with stellar activity cycles are plotted with their cycle amplitude as a function of fundamental stellar properties: T_{eff} , $\log(g)$, $[\text{Fe}/\text{H}]$, and $\log(R'_{\text{HK}})$ (panels (A), (B), (C), and (D), respectively). The derived parameters of M_* , R_* , chromospheric age, and activity-derived rotation period are plotted in panels (E), (F), (G), and (H), respectively. Age uncertainties are 60% (Mamajek & Hillenbrand 2008). Orange crosses highlight solar-type stars with $5600 \text{ K} < T_{\text{eff}} < 5900 \text{ K}$. Pink stars have T_{eff} less than 4700 K . Note their distinct parameter space from the FGK stars. The ages and rotation periods for these cooler stars are not well calibrated with activity and are only shown for completeness. Cycle amplitudes are S -value peak amplitudes, not peak-to-peak. HD 38529 with a radius of $2.5 R_{\odot}$ is not shown in panel (F).

mechanism would generate magnetic activity. We find one such star with a cycle, HD 210302 (5.7 yr, $T_{\text{eff}} = 6385 \text{ K}$). The S -value standard deviation is 0.0021 and the cycle amplitude is 0.160,

placing the amplitude of this cycle near the limit of detection. Most stars with $T_{\text{eff}} > 6000 \text{ K}$ have an S -value rms less than 0.002, the threshold below which we do not search for cycles.

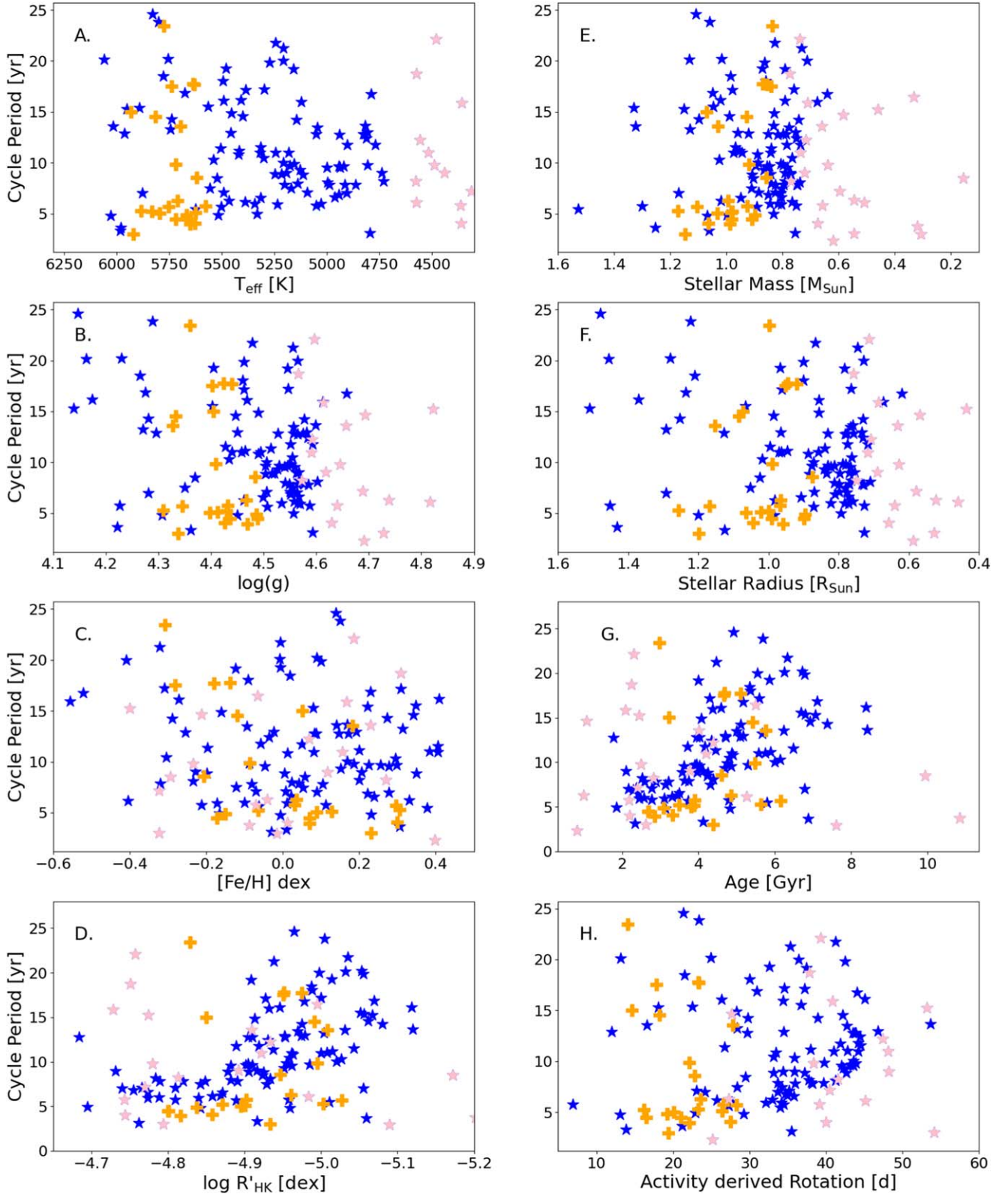


Figure 12. Stars with stellar activity cycles are plotted with their cycle period as a function of their fundamental stellar properties T_{eff} , $\log(g)$, $[\text{Fe}/\text{H}]$, and $\log(R'_{\text{HK}})$ (panels (A), (B), (C), and (D), respectively) and derived parameters M_* , R_* , chromospheric age, and chromospheric rotation period (panels (E), (F), (G), and (H)). Orange crosses highlight solar-type stars with $5600 \text{ K} < T_{\text{eff}} < 5900 \text{ K}$. Stars with $T_{\text{eff}} < 4700 \text{ K}$ are plotted in pink. Note their distinct parameter space from the FGK stars. The ages and rotation periods for these cooler stars are not well calibrated and are only shown for completeness.

5.8. Candidate Cycles

The choice of number of observations and the model selection drive our detection thresholds. While well-sampled stars with

high-amplitude signals are straightforward to identify with numeric thresholds, those on the margin of detection, near the detection thresholds, or with poor sampling may not be

considered cycling stars when additional observations are added or new detection methods are used such as the Fourier transform and the Choi–Williams distribution used in Oláh et al. (2016).

Some candidate cycles include HD 188015, which has a strong peak in the periodogram at 11 yr, but has only 38 observations. This shows that some of our declared cycles may not pass future thresholds, and others will be added to the cycling-star catalogs in the future. We do not identify linear trends, which are likely indications of cycles with periods beyond our baseline.

6. Discussion

6.1. Our Assessment

The changing nature of a star’s cycle is impossible to observe over megayear to gigayear timescales. By collecting vignettes of hundreds of similar stars over several decades, we can piece together their long-term behavior. Observations of the solar cycle have been collected over hundreds of years, covering dozens of solar cycles. The nature of the solar cycle has been explored by observing solar-like stars’ chromospheric activity on yearly and decades-long timescales. The dedicated long-term observing programs that have enabled the collection of data sets that cover 20, 30, and 40 yr have proven invaluable in revealing the evolution of stellar activity cycles.

High-resolution spectroscopy has contributed to these studies through time-series observations, primarily to find and characterize extrasolar planets. Ca II H and K time series are collected alongside RV measurements to decorrelate RVs from stellar activity (Mayor & Queloz 1995). The CLS provides 20 yr observing baselines for 285 stars (710 on shorter baselines) on a single instrument. Planet search spectroscopy also allows determination of precise stellar properties, which have been used effectively to search for subtle trends in exoplanet demographics (Fulton & Petigura 2018).

Using the activity time series and precise stellar properties we identify a range of stellar activity in which nearly every star is cycling. Refined $B - V$ values that are calculated from T_{eff} and $[\text{Fe}/\text{H}]$ and are homogeneously determined are required for identifying the $\log(R'_{\text{HK}})$ range on the main sequence for G- and K-type stars in which the period of the cycle is tightly correlated to the effective temperature. In the T_{eff} range of 4700–5900 K and the $\log(R'_{\text{HK}})$ range between -4.7 and -4.9 , we find the cycle period increases as T_{eff} decreases. And for stars less active than $\log(R'_{\text{HK}}) = -4.9$, the correlation does not hold, and T_{eff} is no longer closely related to the cycle period.

As young, active stars with $\log(R'_{\text{HK}})$ more than -4.7 spin down and expel their angular momentum, their cycles become detectable as they begin to have a more periodic nature. Prior to reaching the steady state of cycling these stars are likely categorized as “active/variable” in studies such as Baliunas et al. (1995) and Baum et al. (2022). Their stellar cycles may be present but they are less sinusoidal and their period is inconsistent from one cycle to the next. The activity level at which stars transition from irregular to regular cycle periods is different for different T_{eff} . For Sunlike stars [5600, 5900] the cycles become regularly periodic around -4.80 . For the next three bins of temperature, [5300, 5600], [5000, 5300], and [4700, 5000], the first periodic cycles are identified at -4.70 , -4.76 , and -4.7 . The trends described in these temperature bins hold for the stars between [5900, 6300], but the bin has only 10 stars. The least active star with a cycle has a $\log(R'_{\text{HK}}) = -4.85$.

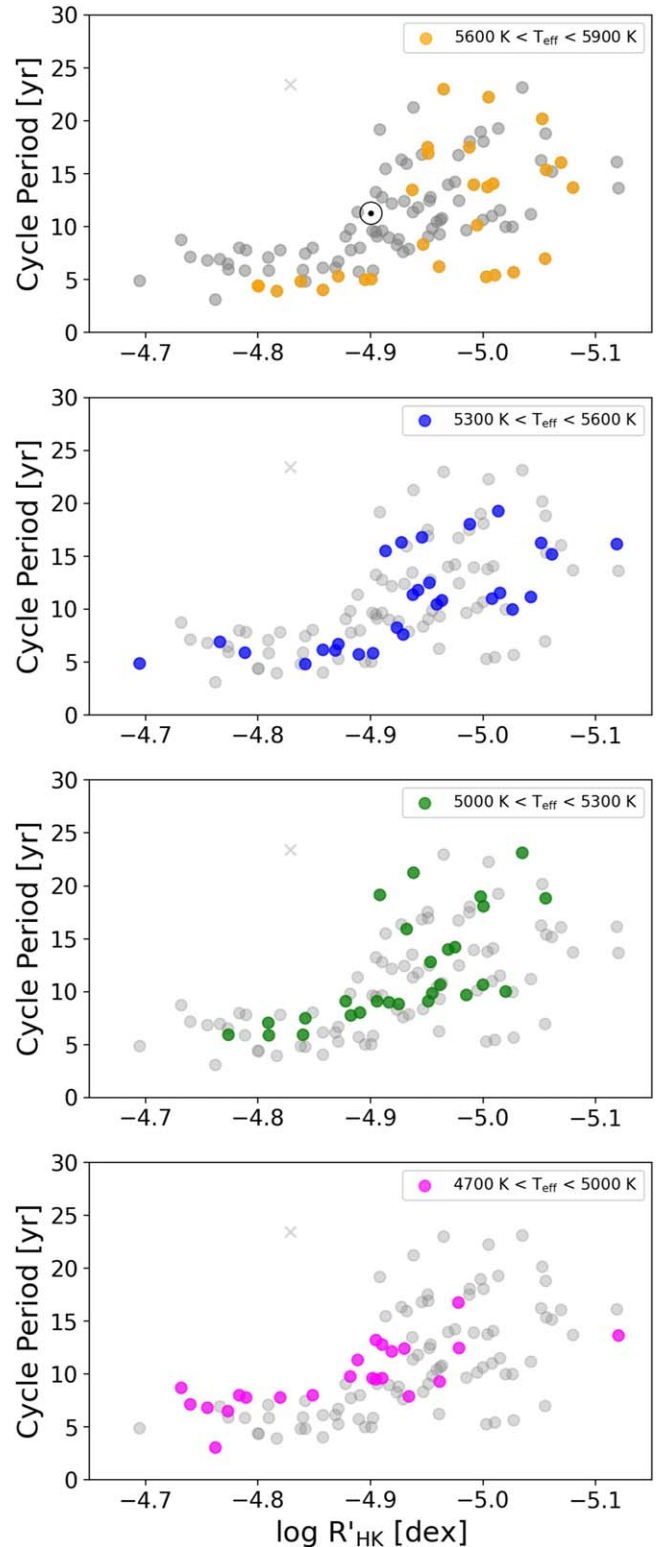


Figure 13. Stellar activity cycle period is presented as a function of chromospheric activity $\log(R'_{\text{HK}})$ for different temperature ranges. The Sun is placed at $\log(R'_{\text{HK}})$ of -4.9 and an 11 yr cycle period. The average cycle period increases at all activity levels for every temperature bin. In the range of $\log(R'_{\text{HK}})$ between -4.7 and -4.9 , 33/42 stars have cycles. In each specified range of T_{eff} and activity, the cycle period is tightly grouped. The gray data points represent all stars between [4700, 5900].

Figure 13 shows the relationship between $\log(R'_{\text{HK}})$ and cycle periods for ranges of temperature in 300 K bins, revealing the transition of cycle period trends at a $\log(R'_{\text{HK}})$ value near

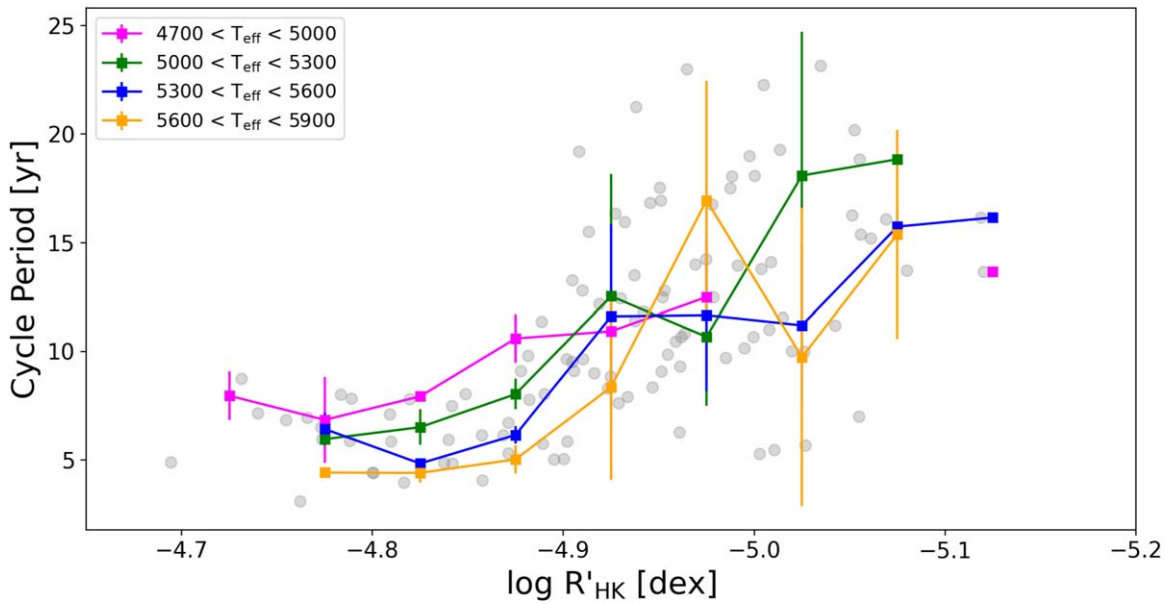


Figure 14. The average cycle period and the cycle period scatter increase for every temperature bin at $\log(R'_{\text{HK}}) = -4.90$. For more active stars, cycle period and T_{eff} are tightly coupled. For less active stars, cycle period is not related to T_{eff} . The bin size is 0.05 and error bars represent the standard deviation in each temperature/activity bin.

–4.9. Divided at –4.9, more active stars have tightly grouped periods for each temperature range and the correlation disappears for less active stars. If we consider the stars more active than $\log(R'_{\text{HK}})$ of –4.9, we find that in the solar temperature bin, cycles are $4.4 \text{ yr} \pm 0.5 \text{ yr}$. From 5300 to 5600 K cycles are $6.0 \text{ yr} \pm 0.7 \text{ yr}$. From 5000 to 5300 K cycles are $7.2 \text{ yr} \pm 1.1 \text{ yr}$. From 4700 to 5000 K cycles are $7.8 \text{ yr} \pm 2.0 \text{ yr}$.

For stars less active than $\log(R'_{\text{HK}})$ of –4.9, activity and cycle period decorrelate and the deterministic nature of cycle period as a function of $\log(R'_{\text{HK}})$ no longer holds. Cycle periods and standard deviation values are, from the hottest to the coolest bin, $13.7 \pm 5.6 \text{ yr}$, $11.7 \pm 3.6 \text{ yr}$, $12.8 \pm 4.6 \text{ yr}$, and $12.2 \pm 2.4 \text{ yr}$. In Figure 14, we average the cycle periods in bin sizes of 0.05 and plot the median with the standard deviation in each bin as an error bar, revealing a small scatter and tightly correlated cycle periods. The transition to longer periods as a function of activity occurs near $\log(R'_{\text{HK}}) = -4.9$.

Of the 42 stars in this temperature–activity range, 33 stars have confirmed cycles. The remaining nine stars have candidate activity cycles with signals that do not meet our threshold requirement or periodogram peak power. Some of them do not have the periods we expect from this newly discovered correlation. We consider this tentative evidence that every star with T_{eff} between 4700 and 5900 K passes through a phase in which a strongly periodic signal exists within a narrow range of periods, and this period is a function of temperature. For this to be true, we must explain why there are no cycles in these nine exceptional stars.

The stars with T_{eff} between 4700 and 5900 K and $\log(R'_{\text{HK}})$ between –4.7 and –4.9 that do not have cycles that pass our threshold are HD 159222, HD 185414, HD 176377, HD 68017, HD 37124, HD 51419, HD 212291, HD 23356, and HD 92719. HD 159222 ($T_{\text{eff}} = 5876 \text{ K}$) has a 3.1 yr candidate cycle that passes our threshold but has a secondary peak that strikes it from our final list of cycles. HD 185414 ($T_{\text{eff}} = 5845 \text{ K}$) has a candidate period at 10 yr, but its periodogram peak of 0.40 falls below our threshold of 0.5. HD 176377 ($T_{\text{eff}} = 5804 \text{ K}$) has a candidate cycle at 4.8 yr but its

periodogram peak of 0.41 falls below our threshold. If future observations confirm this cycle, the cycle period would be consistent with our trend. HD 68017 ($T_{\text{eff}} = 5712 \text{ K}$) has a candidate cycle at 1.1 yr and is slightly less active in terms of both the median S -value and the S -value standard deviation. This star is potentially slightly more evolved than the others. A 1.1 yr cycle would not fit our trend. HD 37124 ($T_{\text{eff}} = 5698 \text{ K}$) has a potential cycle of 22.6 yr, but the cycle is not closed and the periodogram peak is ambiguous to higher periods, so we consider this a lower limit. It also has a slightly lower $\log(g)$ than the other stars discussed here. HD 51419 ($T_{\text{eff}} = 5775 \text{ K}$), marked with an X in Figure 13, is very similar to HD 37124 in that the cycle is not closed and the peak at 23.4 yr is not unique, providing only a lower limit on the period. Its $\log(g)$ value is 4.36. HD 212291 ($T_{\text{eff}} = 5589 \text{ K}$) has two strong peaks in the periodogram, at 4.9 and 5.6 yr, therefore the period is not uniquely determined. Further observations would likely confirm the period and it would fall into our expected trend. HD 23356 ($T_{\text{eff}} = 4976 \text{ K}$) has a candidate signal at 5.4 yr, but it is only identified after removing a linear trend, and even then it does not pass our periodogram peak threshold. If this cycle were confirmed, it would fit our trend. HD 92719 ($T_{\text{eff}} = 5774 \text{ K}$) has a cycle at 4.6 yr, but has an ambiguous period, with a second periodogram peak, removing it from our list.

For those stars in this exception list that do not have candidate cycles, which could be confirmed with more observations, possible explanations include an undervalued T_{eff} , which could shift the star into the $\log(R'_{\text{HK}})$ range where we do not expect a cycle. This possibility is supported by the notion that the coolest star without an expected cycle has a T_{eff} of 5589 K, meaning every star below this value has a cycle within $\log(R'_{\text{HK}})$ of –4.7 to –4.9. Another possibility is a pole-on orientation for these stars.

One star, HD 130992 ($T_{\text{eff}} = 4796 \text{ K}$), has a cycle of period 3.1 yr, going against our trend. We find the poor sampling of this star contributes to its potentially false detection, but it

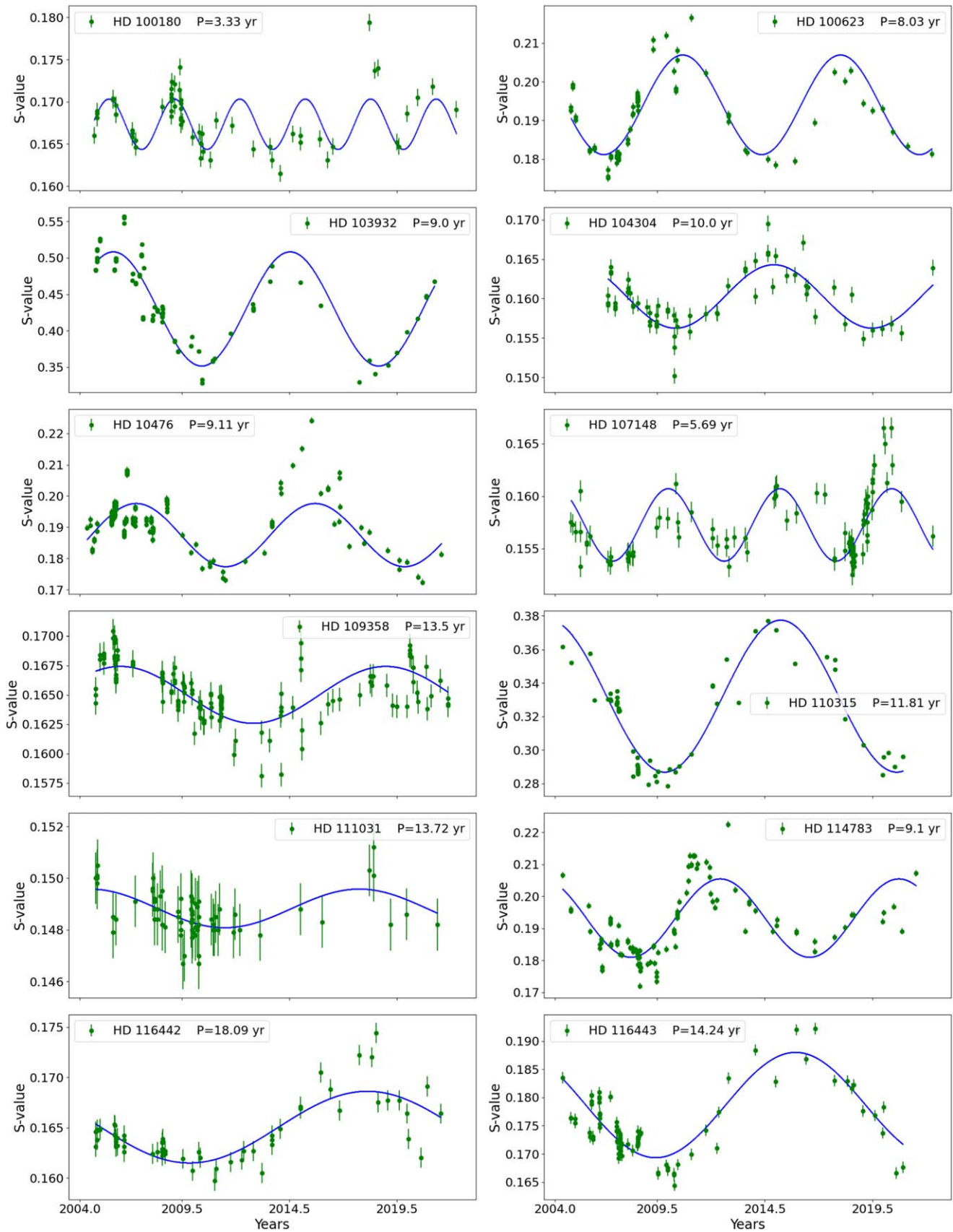


Figure 15. Cycles for stars HD 100180, HD 100623, HD 103932, HD 104304, HD 10476, HD 107148, HD 109358, HD 110315, HD 111031, HD 114783, HD 116442, and HD 116443. The complete figure set contains plots for all 710 stellar activity cycles in our sample. (The complete figure set (60 images) is available in the [online article](#).)

passes all of our numerical thresholds so we include it in our table.

With the possible explanations as to why these eight stars do not have cycles, we again pose the possibility that every star from T_{eff} 4700 to 5900 K and with $\log(R'_{\text{HK}})$ between -4.7 and -4.9 has a regularly periodic activity cycle with a period correlated to T_{eff} . Each of the 138 stars with cycles identified in this work is presented in Figure 15's figure set.

6.2. The Path Forward

Our collection of magnetic activity cycles, found via multi-decade ground-based monitoring of stars in the solar neighborhood, sets the stage for further studies of magnetic activity, rotation, and age.

When considering this specific temperature range, no restrictions are placed on $\log(g)$ or $[\text{Fe}/\text{H}]$. Stellar evolution becomes a factor only after activity values decrease beyond $\log(R'_{\text{HK}})$ of -4.9 , near the Sun's activity level, at which point the changes we observe in activity cycle period become a combination of main-sequence activity changes and evolution of stars off the main sequence. Spectropolarimetry of solar-type stars with different Rossby numbers (Metcalf et al. 2023, 2024) is shown to support the theory of weakened magnetic braking. Adding the findings presented in this work may add to our understanding of the Sun's activity cycle relative to other solar-type stars.

Many stars have previously noted double periods and the ratio of these periods is a strong function of T_{eff} . The Keck/HIRES time baseline of 20 yr is sensitive to cycles with a period of 25 yr, but identifying a second cycle per star will require a different method and threshold of detection. When analyzing stars with two cycles, most previous studies have relied on the Rossby number, the ratio of the rotation period to the convective turnover time (Mittag et al. 2023). In this work, we notably have identified this range of consistent, predictable stellar cycle periods without knowing the stellar rotation periods.

Perhaps the most intriguing question around stellar activity cycles and rotation periods is what happens to solar-type stars as their dynamo transitions from having a strong relationship between rotation, age, and activity. For old main-sequence stars, there is a breakdown between the rotation period and stellar age, but perhaps not between the overall chromospheric activity and the age of the star. The evolution of stars off the main sequence also clouds the interpretation of these relationships. The homogeneously determined stellar parameters from CLS1 have been used to disentangle such effects (David et al. 2022). The theory of weakened magnetic braking (van Saders et al. 2016; Metcalfe et al. 2022) is supported by the measurements of stellar rotation periods with Kepler photometry and independently with asteroseismically determined rotation periods. We present another independent data set that can be used to test weakened magnetic braking.

The examination of magnetic cycles as a function of age (Oláh et al. 2016) provides a path forward for future studies that can take advantage of large time series of Ca II H and K activity measurements. Figure 12 shows that the regularly cycling stars correspond to chromospheric ages between 2 and 4 Gyr. Using independently determined ages makes this conjecture more reliable. Adding measurements of rotational modulation and age to the data presented here will further

elucidate the relationship between the magnetic activity of stars and their observable proxies. Examination of the ratio of rotation period to activity cycle for the Mount Wilson sample shows both consistency with previous studies and subtlety in the dependence on stellar temperature (Mittag et al. 2023). The larger sample of cycles presented here, with precise stellar properties, provides an opportunity to further study these relationships and their impact on stellar dynamos.

This new collection of stellar activity cycles, with its broad span in terms of stellar T_{eff} and $\log(g)$, can be used to broaden the connections between stellar cycle periods and theoretical understandings of the generation of magnetic fields in stars. We defer the analysis of ages, rotation periods, and Rossby numbers to future studies, noting specifically that the Rossby number is not required in our current analysis. We identify the trend between cycle period and T_{eff} and the transition from a strongly correlated period to a weak correlation with only activity time series.

7. Conclusion

We present the largest sample of spectroscopically determined stellar activity cycles to date, with optical spectroscopy of 710 solar neighborhood stars collected over two decades to catalog chromospheric activity, and search for stellar activity cycles. The CLS stars forming the basis of this survey may also aid exoplanet RV surveys. The Ca II H and K time-series data serves as a proxy for stellar and chromospheric activity, measurements that can be utilized in the detection and characterization of exoplanets.

From our Keck/HIRES Ca II H and K data set, a total of 285 stars are amenable to searches for stellar cycles with periods ranging from 2 to 25 yr, and 138 stars show stellar cycles of varying length and amplitude. These activity cycle observations in turn may be used to disentangle the effect of stellar magnetic activity when detecting and characterizing exoplanets.

The results presented may also find use in placing the Sun's stellar magnetic activity within the context of the activity of solar neighborhood stars, including an improved understanding of stellar activity through the star's main-sequence lifetime.

The collection of Ca II H and K measurements from the Mount Wilson Observatory HK Project helped to place the solar cycle into context in the solar neighborhood. The empirical identification of cycles and rotation periods, along with the theoretical underpinnings of convective turnover times and mixing lengths, has greatly improved the understanding of magnetic phenomena on and below the stellar surface. Folding stellar age into what we know about activity cycles and rotation may lead to deeper understanding of the changes in stars' chromospheric activity on gigayear timescales.

Finally, we provide tentative evidence that every G- and K-type star passes through a stage of stellar activity in which stellar activity cycles are present and their period is strongly correlated to the effective temperature.

Acknowledgments

We thank Daniel Huber, Simon Albrecht, Simon Murphy, and Aaron Householder for helpful comments, and Lee Rosenthal for his early work on CLS. And we thank the anonymous referee for constructive feedback during review.

This work was supported by NASA Keck PI Data Awards, administered by the NASA Exoplanet Science Institute. Some of the data presented herein were obtained at the W. M. Keck Observatory, which is operated as a scientific partnership among the California Institute of Technology, the University of California, and the National Aeronautics and Space Administration. The Observatory was made possible by the generous financial support of the W. M. Keck Foundation. This research made use of NASA's Astrophysics Data System.

This project would not have been possible without major allocations of Keck telescope time from the University of California, the California Institute of Technology, the University of Hawaii, and NASA. This work utilized the SIMBAD astronomical database.

Author contributions: H.I. conducted the analysis and wrote the paper. A.W.H. was an originator of the survey. B.F., E.A.P., and L.M.W. are original collaborators on CLS. S.R.K. and B.C. advised on the analysis. Authors C.B. to N.S. in the author list above provided comments on the paper and contributed to the observing effort in order of their appearance.



The data collected here, previously published and novel, was gathered on over 1500 individual nights by 152 unique observers. Without their contribution to astronomical data collection, this work would not be possible.










The authors wish to recognize and acknowledge the very significant cultural role and reverence that the summit of Maunakea has always had within the indigenous Hawaiian community. We are most fortunate to have the opportunity to conduct observations from this mountain.

Facility: Keck:I (HIRES)

Software: We made use of the following publicly available Python modules: Astropy (Astropy Collaboration et al. 2013, 2018, 2022), matplotlib (Hunter 2007), numpy (van der Walt et al. 2011), scipy (Virtanen et al. 2020), and pandas (McKinney 2010). IDL was used to extract the spectral line information (ENVI version 4.8; Exelis Visual Information Solutions, Boulder, Colorado).

ORCID iDs

Howard Isaacson  <https://orcid.org/0000-0002-0531-1073>
 Andrew W. Howard  <https://orcid.org/0000-0001-8638-0320>
 Benjamin Fulton  <https://orcid.org/0000-0003-3504-5316>
 Erik A. Petigura  <https://orcid.org/0000-0003-0967-2893>
 Lauren M. Weiss  <https://orcid.org/0000-0002-3725-3058>
 Stephen R. Kane  <https://orcid.org/0000-0002-7084-0529>
 Corey Beard  <https://orcid.org/0000-0001-7708-2364>
 Steven Giacalone  <https://orcid.org/0000-0002-8965-3969>
 Judah Van Zandt  <https://orcid.org/0000-0002-4290-6826>
 Joseph M. Akana Murphy  <https://orcid.org/0000-0001-8898-8284>
 Fei Dai  <https://orcid.org/0000-0002-8958-0683>
 Ashley Chontos  <https://orcid.org/0000-0003-1125-2564>
 Alex S. Polanski  <https://orcid.org/0000-0001-7047-8681>
 Malena Rice  <https://orcid.org/0000-0002-7670-670X>
 Jack Lubin  <https://orcid.org/0000-0001-8342-7736>
 Casey Brinkman  <https://orcid.org/0000-0002-4480-310X>
 Ryan A. Rubenzahl  <https://orcid.org/0000-0003-3856-3143>
 Sarah Blunt  <https://orcid.org/0000-0002-3199-2888>
 Samuel W. Yee  <https://orcid.org/0000-0001-7961-3907>
 Mason G. MacDougall  <https://orcid.org/0000-0003-2562-9043>
 Paul A. Dalba  <https://orcid.org/0000-0002-4297-5506>
 Dakotah Tyler  <https://orcid.org/0000-0003-0298-4667>

Isabel Angelo  <https://orcid.org/0000-0002-9751-2664>
 Daria Pidhorodetska  <https://orcid.org/0000-0001-9771-7953>
 Andrew W. Mayo  <https://orcid.org/0000-0002-7216-2135>
 Rae Holcomb  <https://orcid.org/0000-0002-5034-9476>
 Emma V. Turtelboom  <https://orcid.org/0000-0002-1845-2617>
 Michelle L. Hill  <https://orcid.org/0000-0002-0139-4756>
 Luke G. Bouma  <https://orcid.org/0000-0002-0514-5538>
 Jingwen Zhang  <https://orcid.org/0000-0002-2696-2406>
 Nicholas Saunders  <https://orcid.org/0000-0003-2657-3889>

References

- Angus, R., Morton, T., Aigrain, S., Foreman-Mackey, D., & Rajpaul, V. 2018, *MNRAS*, 474, 2094
- Astropy Collaboration, Price-Whelan, A. M., Lim, P. L., et al. 2022, *ApJ*, 935, 167
- Astropy Collaboration, Price-Whelan, A. M., Sipőcz, B. M., et al. 2018, *AJ*, 156, 123
- Astropy Collaboration, Robitaille, T. P., Tollerud, E. J., et al. 2013, *A&A*, 558, A33
- Astudillo-Defru, N., Forveille, T., Bonfils, X., et al. 2017, *A&A*, 602, A88
- Baliunas, S. L., Donahue, R. A., Soon, W. H., et al. 1995, *ApJ*, 438, 269
- Barnes, S. A. 2007, *ApJ*, 669, 1167
- Baum, A. C., Wright, J. T., Luhn, J. K., & Isaacson, H. 2022, *AJ*, 163, 183
- Boro Saikia, S., Marvin, C. J., Jeffers, S. V., et al. 2018, *A&A*, 616, A108
- Bowens-Rubin, R., Akana Murphy, J. M., Hinz, P. M., et al. 2023, *AJ*, 166, 260
- Chen, Y., King, J. R., & Boesgaard, A. M. 2014, *PASP*, 126, 1010
- Cincunegui, C., Díaz, R. F., & Mauas, P. J. D. 2007, *A&A*, 469, 309
- David, T. J., Angus, R., Curtis, J. L., et al. 2022, *ApJ*, 933, 114
- Dragomir, D., Kane, S. R., Henry, G. W., et al. 2012, *ApJ*, 754, 37
- Duncan, D. K., Vaughan, A. H., Wilson, O. C., et al. 1991, *ApJS*, 76, 383
- Eberhard, G., & Schwarzschild, K. 1913, *ApJ*, 38, 292
- Fischer, D. A., Marcy, G. W., & Spronck, J. F. P. 2014, *ApJS*, 210, 5
- Flores, M., González, J. F., Jaque Arancibia, M., Buccino, A., & Saffe, C. 2016, *A&A*, 589, A135
- Fuhrmeister, B., Coffaro, M., Stelzer, B., et al. 2023, *A&A*, 672, A149
- Fulton, B. J., & Petigura, E. A. 2018, *AJ*, 156, 264
- Fulton, B. J., Rosenthal, L. J., Hirsch, L. A., et al. 2021, *ApJS*, 255, 14
- Fulton, B. J., Weiss, L. M., Sinukoff, E., et al. 2015, *ApJ*, 805, 175
- Gomes da Silva, J., Santos, N. C., Adibekyan, V., et al. 2021, *A&A*, 646, A77
- Hall, J. C., Lockwood, G. W., & Skiff, B. A. 2007, *AJ*, 133, 862
- Henry, T. J., Soderblom, D. R., Donahue, R. A., & Baliunas, S. L. 1996, *AJ*, 111, 439
- Howard, A. W., Johnson, J. A., Marcy, G. W., et al. 2010, *ApJ*, 721, 1467
- Hunter, J. D. 2007, *CSE*, 9, 90
- Irving, Z. A., Saar, S. H., Wargelin, B. J., & do Nascimento, J.-D. 2023, *ApJ*, 949, 51
- Isaacson, H., & Fischer, D. 2010, *ApJ*, 725, 875
- Jeffers, S. V., Kiefer, R., & Metcalfe, T. S. 2023, *SSRv*, 219, 54
- Johnson, M. C., Endl, M., Cochran, W. D., et al. 2016, *ApJ*, 821, 74
- Joyce, M., & Chaboyer, B. 2018, *ApJ*, 856, 10
- Kane, S. R. 2023, *AJ*, 166, 187
- Kane, S. R., Thirumalachari, B., Henry, G. W., et al. 2016, *ApJL*, 820, L5
- Kraft, R. P. 1967, *ApJ*, 150, 551
- Lovis, C., Dumusque, X., Santos, N. C., et al. 2011, arXiv:1107.5325
- Lubin, J., Robertson, P., Stefansson, G., et al. 2021, *AJ*, 162, 61
- Luhn, J. K., Wright, J. T., Henry, G. W., Saar, S. H., & Baum, A. C. 2022, *ApJL*, 936, L23
- Luhn, J. K., Wright, J. T., Howard, A. W., & Isaacson, H. 2020, *AJ*, 159, 235
- Mamajek, E. E., & Hillenbrand, L. A. 2008, *ApJ*, 687, 1264
- Marcy, G. W., Isaacson, H., Howard, A. W., et al. 2014, *ApJS*, 210, 20
- Marsden, S. C., Petit, P., Jeffers, S. V., et al. 2014, *MNRAS*, 444, 3517
- Marvin, C. J., Reiners, A., Anglada-Escudé, G., Jeffers, S. V., & Boro Saikia, S. 2023, *A&A*, 671, A162
- Mayor, M., & Queloz, D. 1995, *Natur*, 378, 355
- McKinney, W. 2010, in Proc. of the 9th Python in Science Conf., ed. W. Stéfan van der & M. Jarrod, 56
- McQuillan, A., Mazeh, T., & Aigrain, S. 2014, *ApJS*, 211, 24
- Metcalfe, T. S., Buccino, A. P., Brown, B. P., et al. 2013, *ApJL*, 763, L26
- Metcalfe, T. S., Finley, A. J., Kochukhov, O., et al. 2022, *ApJL*, 933, L17
- Metcalfe, T. S., Strassmeier, K. G., Ilyin, I. V., et al. 2023, *ApJL*, 948, L6
- Metcalfe, T. S., Strassmeier, K. G., Ilyin, I. V., et al. 2024, *ApJL*, 960, L6

- Mittag, M., Schmitt, J. H. M. M., & Schröder, K. P. 2013, *A&A*, **549**, A117
- Mittag, M., Schmitt, J. H. M. M., & Schröder, K. P. 2023, *A&A*, **674**, A116
- Noyes, R. W., Hartmann, L. W., Baliunas, S. L., Duncan, D. K., & Vaughan, A. H. 1984, *ApJ*, **279**, 763
- Obridko, V. N., Katsova, M. M., & Sokoloff, D. D. 2022, *MNRAS*, **516**, 1251
- Oláh, K., Kővári, Z., Petrovay, K., et al. 2016, *A&A*, **590**, A133
- Perdelwitz, V., Mittag, M., Tal-Or, L., et al. 2021, *A&A*, **652**, A116
- Petigura, E. A., Howard, A. W., Marcy, G. W., et al. 2017, *AJ*, **154**, 107
- Ramírez, I., & Meléndez, J. 2005, *ApJ*, **626**, 465
- Robertson, P., Endl, M., Cochran, W. D., MacQueen, P. J., & Boss, A. P. 2013, *ApJ*, **774**, 147
- Rosenthal, L. J., Fulton, B. J., Hirsch, L. A., et al. 2021, *ApJS*, **255**, 8
- Savanov, I. S. 2012, *ARep*, **56**, 716
- Schröder, K. P., Mittag, M., Hempelmann, A., González-Pérez, J. N., & Schmitt, J. H. M. M. 2013, *A&A*, **554**, A50
- See, V., Roquette, J., Amard, L., & Matt, S. 2023, *MNRAS*, **524**, 5781
- Shah, S. P., Wright, J. T., Isaacson, H., Howard, A. W., & Curtis, J. L. 2018, *ApJL*, **863**, L26
- Shen, Y.-F., Zhao, G., & Bird, S. A. 2022, *Univ*, **8**, 488
- Suárez Mascareño, A., Rebolo, R., González Hernández, J. I., & Esposito, M. 2015, *MNRAS*, **452**, 2745
- Suárez Mascareño, A., Rebolo, R., & González Hernández, J. I. 2016, *A&A*, **595**, A12
- Suárez Mascareño, A., Rebolo, R., González Hernández, J. I., et al. 2018, *A&A*, **612**, A89
- Toledo-Padrón, B., González Hernández, J. I., Rodríguez-López, C., et al. 2019, *MNRAS*, **488**, 5145
- van der Walt, S., Colbert, S. C., & Varoquaux, G. 2011, *CSE*, **13**, 22
- van Saders, J. L., Ceillier, T., Metcalfe, T. S., et al. 2016, *Natur*, **529**, 181
- Vaughan, A. H., Preston, G. W., & Wilson, O. C. 1978, *PASP*, **90**, 267
- Virtanen, P., Gommers, R., Oliphant, T. E., et al. 2020, *NatMe*, **17**, 261
- Wargelin, B. J., Saar, S. H., Pojmański, G., Drake, J. J., & Kashyap, V. L. 2017, *MNRAS*, **464**, 3281
- Wilson, O. C. 1968, *ApJ*, **153**, 221
- Wright, J. T. 2016, arXiv:1603.08384
- Wright, J. T., Marcy, G. W., Butler, R. P., & Vogt, S. S. 2004, *ApJS*, **152**, 261
- Wright, J. T., Marcy, G. W., Butler, R. P., et al. 2008, *ApJL*, **683**, L63
- Yee, S. W., Petigura, E. A., & von Braun, K. 2017, *ApJ*, **836**, 77